ANNUAL REVIEWS

Annual Review of Condensed Matter Physics

Random Quantum Circuits

Matthew P.A. Fisher,[1] Vedika Khemani,[2] Adam Nahum,[3] and Sagar Vijay[1]

[1]Department of Physics, University of California, Santa Barbara, California, USA; email: mpaf@ucsb.edu, sagarvijay@ucsb.edu

[2]Department of Physics, Stanford University, Stanford, California, USA; email: vkhemani@stanford.edu

[3]Laboratoire de Physique, École Normale Supérieure, CNRS, Université PSL, Sorbonne Université, Université de Paris, Paris, France; email: adam.nahum@phys.ens.fr

Annu. Rev. Condens. Matter Phys. 2023. 14:335–79

First published as a Review in Advance on December 12, 2022

The *Annual Review of Condensed Matter Physics* is online at conmatphys.annualreviews.org

https://doi.org/10.1146/annurev-conmatphys-031720-030658

Keywords

entanglement, nonequilibrium dynamics, quantum simulators, quantum measurements, quantum chaos

Abstract

Quantum circuits—built from local unitary gates and local measurements—are a new playground for quantum many-body physics and a tractable setting to explore universal collective phenomena far from equilibrium. These models have shed light on longstanding questions about thermalization and chaos, and on the underlying universal dynamics of quantum information and entanglement. In addition, such models generate new sets of questions and give rise to phenomena with no traditional analog, such as dynamical phase transitions in quantum systems that are monitored by an external observer. Quantum circuit dynamics is also topical in view of experimental progress in building digital quantum simulators that allow control of precisely these ingredients. Randomness in the circuit elements allows a high level of theoretical control, with a key theme being mappings between real-time quantum dynamics and effective classical lattice models or dynamical processes. Many of the universal phenomena that can be identified in this tractable setting apply to much wider classes of more structured many-body dynamics.

1. INTRODUCTION

Quantum dynamical phenomena, such as the transport of conserved quantities, correlation and response functions of local observables, or dynamics of low-lying excitations, have traditionally been used to probe the universal properties of quantum condensed matter at low temperatures and near equilibrium. In contrast, because quantum coherence is easily destroyed at high temperatures, it might seem that quantum matter evolved far from its ground-state would fail to exhibit universal dynamics that is distinctively quantum. However, efforts to understand out-of-equilibrium dynamics in lattice models (1–18), quantum field theories (19–22), and black holes (23–27) have shown that universal structures can emerge in quantum correlations and in the patterns of quantum entanglement of a many-body system. These structures underlie thermalization, when it occurs, as well as novel forms of nonthermalizing dynamics (1, 2).

The search for universal phenomena in the out-of-equilibrium dynamics of quantum many-body systems has been intensified by efforts at the interface of quantum information science and condensed matter physics to build quantum simulators (28), systems of hundreds of qubits that can realize interesting many-body phases. Analog quantum simulators, such as ultracold atom platforms (29–31), arrays of atoms with long-range interactions that are tuned by excitation into Rydberg states (32), and trapped atomic ions (33, 34), exert control over constituent degrees of freedom by tuning the Hamiltonian governing their interactions. The possibility of highly coherent and controllable Hamiltonian dynamics has led to important questions about universality in the approach to thermal equilibrium (1, 35) and situations in which quenched disorder can arrest thermalization entirely via the phenomenon of many-body localization (MBL; 2, 3, 36).

Recently developed digital quantum simulators afford an even greater degree of control. The native mode of operation of these platforms, such as those formed of superconducting qubits (37, 38), involves the discrete time evolution of constituent qubits through the application of unitary operations, measurements, and feedback. Harnessing these ingredients to control quantum many-body systems is a new goal of quantum condensed matter physics. Successful implementation of these operations is also a stepping stone toward the separate goal of eventually building a fault-tolerant quantum computer (39). The advent of digital quantum simulators has thus led to an important question for condensed matter physics: What collective quantum phenomena, or dynamical phases of matter, can emerge using operations—such as unitary gates, measurements, and feedback—that are native to quantum simulators?

This article is an introduction to simple discrete time models for many-body dynamics that have allowed progress on some of these questions. In these models, a lattice of spins (qubits) evolves through the application of local unitary gates and measurements. This discrete time structure—a so-called quantum circuit (40)—is reminiscent of the "Trotterization" of a continuous-time Hamiltonian evolution, though the time step here is not assumed to be infinitesimal, as each local operation is generally not close to the identity (which also means that energy is not conserved).

A minimally structured unitary quantum circuit that lacks any symmetries or other special properties rapidly brings the system into a steady state that is locally completely disordered, in the sense that local observables reproduce an infinite-temperature statistical ensemble. The search for universal phenomena in this setting thus requires going beyond traditional probes of quantum condensed matter involving correlations between specially chosen local operators. Instead, interesting universal features of the evolving state can be usefully quantified with information-theoretic quantities such as the entanglement entropy and the quantum mutual information; these are measures of correlations that are nonlinear in the reduced density matrix for a subsystem. These observables are also natural in the minimal circuit setting because they are independent of the local choice of basis while remaining sensitive to basic structural features of the dynamics such as locality and unitarity. What universal structures govern the behavior of such observables

in a minimal quantum circuit dynamics? What additional universal phenomena emerge in the presence of further structure and symmetries?

Focusing on these abstract measures of correlation is not an esoteric exercise; measures of entanglement are of particular importance in light of recent developments in condensed matter physics and quantum information science. First, closed quantum systems can reach a local, thermal equilibrium under purely unitary evolution, and understanding the locally irreversible nature of this process of thermalization (41–43) requires studying the production of quantum many-body entanglement. Second, just as patterns of entanglement in equilibrium matter contain universal structures that are characteristic of phases and phase transitions (20, 44–46), entanglement is also an organizing principle for out-of-equilibrium quantum matter. It is interesting to compare universal patterns of entanglement that emerge in this setting with what we know to be possible in equilibrium. Finally, validating the performance of near-term quantum computers requires understanding and executing tasks that we know to be quantifiably hard to perform on a classical computer (47). Quantum information-theoretic quantities (e.g., measures of state and operator entanglement) provide proxies for certain kinds of classical hardness, so that—in addition to shedding light on how to make classical algorithms more efficient—they can be used to pinpoint dynamical regimes where quantum simulation has a genuine advantage.

Significant theoretical progress is possible by incorporating randomness in the allowed local operations that form a quantum circuit. Ensembles of random quantum circuits provide a theoretically tractable setting in which to understand universal out-of-equilibrium phenomena that also occur in more structured quantum many-body dynamics. This is similar in spirit to the role of randomness in, for example, applications of random matrix theory (RMT) to level statistics or mesoscopic transport (48, 49). Loosely speaking, randomness in a quantum circuit allows for a classical description of the evolving entanglement structure in a typical realization of the quantum many-body dynamics (17, 50–52). This result can be heuristically understood by noting that basic observables (both simple correlation functions and entanglement quantities that are nonlinear in the density matrix) are related to probability amplitudes for evolving several copies of the original quantum many-body system into a particular final state. Randomness allows one to show that this evolution is quantum mechanically incoherent. The resulting classical statistical ensemble of Feynman trajectories of the multicopy system exhibits universal properties that reflect quantum correlations in the original system of interest. A key approach taken in this article is to investigate the universal structures that emerge in these classical descriptions and to use these as a foothold for understanding more structured quantum many-body evolution.

We discuss both unitary circuit dynamics and monitored dynamics in which the system's local degrees of freedom are repeatedly measured by an external observer (a nonunitary operation). One way to motivate unitary circuits is as models in which to get analytical control on questions about out-of-equilibrium dynamics and chaos that are equally relevant to more conventional condensed matter models. Monitored circuits, by contrast, show us that new dynamical universality classes are possible (even for dynamics with very little structure) once we step outside the domain of unitary evolution. In particular, we focus on a phase transition, from an entangled to a disentangled phase, induced by monitoring (53, 54). Unitary or weakly monitored dynamics generates complex, highly entangled wave functions, but sufficiently frequent measurement can trap the evolving wave function close to the space of product states. The phases and transitions can again be fruitfully mapped to an effective classical statistical mechanics model (55–58). Monitored many-body systems have been the subject of much recent progress (55, 56, 58–92). We also direct the reader to a recent review (18) on entanglement dynamics in circuits, which gives a useful treatment of many of the same topics we discuss.

This article is organized as follows. In Section 2, we review the fundamental building blocks of quantum circuits along with the two broad classes of quantum circuit dynamics that we study, and we outline some basic physical properties of the circuits. Section 3 focuses on the first class, quantum circuits with local unitary gates. We review a universal description of entanglement growth in this setting and elucidate the structure of correlation functions. We then explore circuits with additional structure beyond locality and unitarity, such as charge-conserving circuits with a hydrodynamic mode, and Floquet circuits with discrete time-translation symmetry. In Section 4, we explore a novel class of open quantum systems that are monitored by an observer who makes repeated measurements. We describe hybrid quantum circuits with both unitary gates and measurements, and a phase transition, driven by measurements, in the entanglement structure of the quantum trajectories. We explore properties of the phases and phase transitions in such circuits and also discuss the role of additional structure such as discrete or continuous symmetries. Section 5 discusses some experimental implications, and Section 6 is a brief outlook of open questions and future possible directions.

2. MODELS AND MOTIVATION

We start this section with a pedagogical introduction to the essential building blocks of a quantum circuit at the level of one or two qubits, to develop some intuition for the effect of these ingredients on correlations in a quantum many-body system. We also introduce basis-independent measures of quantum correlations, the entanglement entropy and the bipartite mutual information, which we use throughout this review. Then we define the 1+1-dimensional unitary (Section 2.3) and monitored (Section 2.4) circuits that we consider. In Sections 2.5 and 2.6, we briefly sketch what these circuits can be used to study and some of the structures allowing analytic calculations.

2.1. Circuit Building Blocks and Quantum Entanglement

Throughout this review, we study d-dimensional quantum many-body systems composed of qubits (or more generally, q-level systems qudits) that are arranged in a spatially local fashion. The discrete time evolution of such a quantum many-body system through the application of local operations defines a quantum circuit. We restrict our attention to (*a*) quantum gates acting on a few nearby qubits and, in the second part of this review, also (*b*) local projective measurements. Quantum gates are unitary transformations acting on the qubits. Projective measurements are observations that leave the measured degrees of freedom in an eigenstate of the measured operator. Measurements are inherently stochastic: Identical measurements performed on multiple copies of the same wave function can yield different outcomes, which are distributed according to Born's rule.

We make extensive use of the entanglement entropy (or rather entropies) to quantify correlations in quantum states evolving under these ingredients. Consider a quantum many-body system composed of N qubits and described by a wave function $|\Psi\rangle$, which is bipartitioned into a subset of spins A, with Hilbert space dimension D_A, and its complement $\bar{A}$, with Hilbert space dimension $D_{\bar{A}}$. The entanglement entropy is a measure of the entanglement between A and $\bar{A}$ and also a basis-independent measure of the correlations between these regions. It can be expressed in terms of the reduced density matrix ρ_A, which encodes all expectation values of operators solely within region A. This is given by tracing over the complementary subsystem $\bar{A}$: $\rho_A \equiv \mathrm{Tr}_{\bar{A}} |\Psi\rangle \langle\Psi|$. The eigenvalues $\{\lambda_i\}$ of ρ_A are nonnegative and sum to unity, $\sum_i \lambda_i = 1$, and as we recall below, the number of nonzero eigenvalues is also the number of terms required to write $|\Psi\rangle$ as a superposition of unentangled (product) states.

The von Neumann entanglement entropy is defined as

$$S_A \equiv -\mathrm{Tr}\,(\rho_A \ln \rho_A)\,. \qquad 1.$$

We often consider the nth Rényi entropy $S_A^{(n)} \equiv \ln\left(\mathrm{Tr}\rho_A^n\right)/(1-n)$ as another measure of quantum entanglement, with the von Neumann entropy given by the limit $n \to 1$.

The entanglement entropy can also be used to define a basis-independent measure of correlations between subsystems A and B whose union is not necessarily the entire system. This quantity, the mutual information, is defined as

$$I_{AB} = S_A + S_B - S_{A\cup B}. \qquad 2.$$

The Rényi and von Neumann entropies enjoy a number of important properties:

1. $S_A^{(n)}$ is insensitive to unitary transformations that act separately within A or $\bar{A}$, such as local changes of basis in the quantum many-body system, because these leave the eigenvalues of the reduced density matrix unchanged.
2. $0 \le S_A^{(n)} \le \ln D$, where $D = \min(D_A, D_{\bar{A}})$. $S_A^{(n)}$ is zero if subsystem A is pure and may be described by a single wave function $\rho_A = |\phi\rangle\langle\phi|$ and is maximized if the reduced density matrix for the smaller of the two subsystems is I_D/D, where I_D is the $D \times D$ identity matrix (in this case we say that this subsystem is in a maximally mixed state). In the former case, we say that the two subsystems are disentangled.
3. Writing $\rho_A = \sum_i p_i |\phi_i\rangle\langle\phi_i|$ as a probabilistic mixture of orthonormal pure states (see below), with probabilities $p_i = \lambda_i$, the von Neumann entropy $S_A = -\sum_i p_i \ln p_i$ is the classical Shannon entropy of this distribution.

The von Neumann entropy is often preferred to other Rényi entropies as a measure of entanglement because it satisfies additional properties, such as subadditivity, strong subadditivity, and concavity, which are natural if we wish to give S_A an information-theoretic interpretation (40).[1]

Heuristically, the entanglement entropy between complementary sets of spins A and $\bar{A}$ quantifies (the logarithm of) the number of terms required to write the pure state $|\psi\rangle$ as a superposition of product states between A and $\bar{A}$. Formally, $|\psi\rangle$ may be written in the Schmidt form $|\psi\rangle = \sum_i \sqrt{\lambda_i}\,|\phi_i\rangle_A\,|\chi_i\rangle_{\bar{A}}$, where $|\phi_i\rangle_A$ and $|\chi_i\rangle_{\bar{A}}$ are orthonormal sets of states in the two subsystems, and i runs over at most $\min(D_A, D_{\bar{A}})$ values. The distinct Rényi entropies correspond to distinct counts of the Schmidt values that discount smaller values of λ_i to a greater or lesser extent.

A key point is that low-entanglement states can be expressed (or approximated) by keeping a number of Schmidt states that is much smaller than D. A generalization of this idea to matrix product states (MPSs) for 1D chains means that there is a direct relationship between the entanglement of a 1D quantum state and the cost of storing it as an MPS (94). Related ideas apply also to matrix product operator (MPO) representations of quantum operators.

2.2. Quantum Gates and Measurements: A Two-Qubit Example

To illustrate the effect of the basic building blocks of quantum circuits (quantum gates and measurements) on a quantum state and its entanglement, we consider examples involving only one or two qubits.

Starting with a single qubit, recall that any Hermitian operator acting on the qubit may be written as a linear combination of the three Pauli matrices and the identity operator,

$$X = \begin{bmatrix} 0 & 1 \\ 1 & 0 \end{bmatrix}, \quad Y = \begin{bmatrix} 0 & -i \\ i & 0 \end{bmatrix}, \quad Z = \begin{bmatrix} 1 & 0 \\ 0 & -1 \end{bmatrix}, \quad I = \begin{bmatrix} 1 & 0 \\ 0 & 1 \end{bmatrix}, \qquad 3.$$

[1] Subadditivity means that if a region A is decomposed into regions A_1 and A_2, then $S_A \le S_{A_1} + S_{A_2}$. Heuristically, there is less "uncertainty" in ρ_A than in the combination of reduced states ρ_{A_1} and ρ_{A_2}, because these are fully determined by ρ_A (93).

in the form $\mathcal{O} = \sum_{\mathcal{S}\in\{I,X,Y,Z\}} c_{\mathcal{S}}\mathcal{S} = c_I I + c_X X + c_Y Y + c_Z Z$, where the coefficients in this expansion are given by $c_{\mathcal{S}} = \frac{1}{2}\mathrm{Tr}(\mathcal{S}\mathcal{O})$, with the trace taken over the 2D Hilbert space of the qubit. A unitary acting on the qubit can be written as $u = \exp(-i\sum_{\mathcal{S}\in\{I,X,Y,Z\}} h_{\mathcal{S}}\mathcal{S})$, where the coefficients $h_{\mathcal{S}}$ are real. For a pair of qubits, any Hermitian operator $\mathcal{O}$ may be written as a sum of tensor products of these operators acting on the two qubits. (We write $X_1 = X \otimes I$, etc.)

Consider dynamics of a single spin that interleaves unitary gates and measurements. If the spin is in a pure state, this state is a point on the Bloch sphere, defined by the polarization vector $(\langle X\rangle, \langle Y\rangle, \langle Z\rangle)$. Unitary transformations rotate the state on the Bloch sphere. A measurement, say of Z, causes a stochastic jump to the North or the South Pole, depending on the random measurement outcome (see below for an example in the two-qubit setting). As a result of this randomness, an arbitrary sequence of unitaries and measurements gives a kind of random walk on the Bloch sphere.

For a single spin, all points on the Bloch sphere are equivalent (in the absence of a preferred local basis). But once we have more than one spin, we can distinguish wave functions according to their entanglement. As an illustration, consider a simple process of generation and destruction of entanglement with two qubits. Begin with a state in which both spins are aligned in the Pauli X basis $|\psi\rangle = |\rightarrow\rightarrow\rangle$, so that $X_1|\psi\rangle = |\psi\rangle$ and $X_2|\psi\rangle = |\psi\rangle$, where X_i denotes the Pauli operator X acting on the ith qubit. This state is disentangled because it may be written as a tensor product of the wave function of each spin. We now apply the "controlled–Z" gate acting on both qubits, $\mathrm{CZ} \equiv \exp[i\frac{\pi}{4}(1 - Z_1)(1 - Z_2)]$, so that the new wave function of the two-spin system is

$$|\phi\rangle \equiv \mathrm{CZ}\,|\psi\rangle = \frac{1}{2}\Big[\,|\rightarrow\rightarrow\rangle + |\rightarrow\leftarrow\rangle + |\leftarrow\rightarrow\rangle - |\leftarrow\leftarrow\rangle\,\Big], \qquad 4.$$

where $|\leftarrow\rangle$ is an eigenstate of the Pauli X operator with $X|\leftarrow\rangle = -|\leftarrow\rangle$. It is easily checked that the reduced density matrix for either spin is now maximally mixed, $\rho_{1,2} = I/2$, so that the entanglement entropy for each spin is $\ln 2$.

For most of this review, we discuss generic local unitary gates. The CZ unitary gate that we applied above is in fact nongeneric in two ways. First, it is diagonal in the Pauli Z basis and therefore cannot generate quantum entanglement when acting on product states in this basis. A generic two-qubit quantum gate produces entanglement when acting on any product state of the qubits (though not in general maximal entanglement). The second property is that CZ is a Clifford gate, meaning that it has a simple action on Pauli matrices as we illustrate below. Although the generic gates that we discuss do not have this special property, we describe it here briefly because circuits made of Clifford gates have the important property of being classically simulable (Section 3.3.4).

The initial state $|\psi\rangle$ was stabilized by (invariant under) the Pauli operators X_1 and X_2. An equivalent way to specify the evolved state $|\phi\rangle$ is via the evolution of these operators under the action of the gate, which is given by $\mathrm{CZ}X_1\mathrm{CZ}^\dagger = X_1Z_2$ and $\mathrm{CZ}X_2\mathrm{CZ}^\dagger = Z_1X_2$. These evolved stabilizers uniquely specify the two-qubit wave function, because they satisfy

$$X_1Z_2\,|\phi\rangle = |\phi\rangle \qquad Z_1X_2\,|\phi\rangle = |\phi\rangle. \qquad 5.$$

Here, the Clifford property of CZ has ensured that the evolved stabilizers are simple products of Pauli operators. In contrast, a generic quantum gate evolves a Pauli operator into a sum of products of Pauli operators, as we discuss in Section 3.2.

Finally, a projective measurement of a spin disentangles the measured spin. Starting from the entangled state $|\phi\rangle$, a measurement of X_1 yields the outcomes $X_1 = \pm 1$ with the respective probabilities

$$p_\pm = \langle\phi|\,\mathcal{P}_\pm\,|\phi\rangle = \frac{1}{2}, \qquad \mathcal{P}_\pm \equiv \frac{1 \pm X_1}{2}, \qquad 6.$$

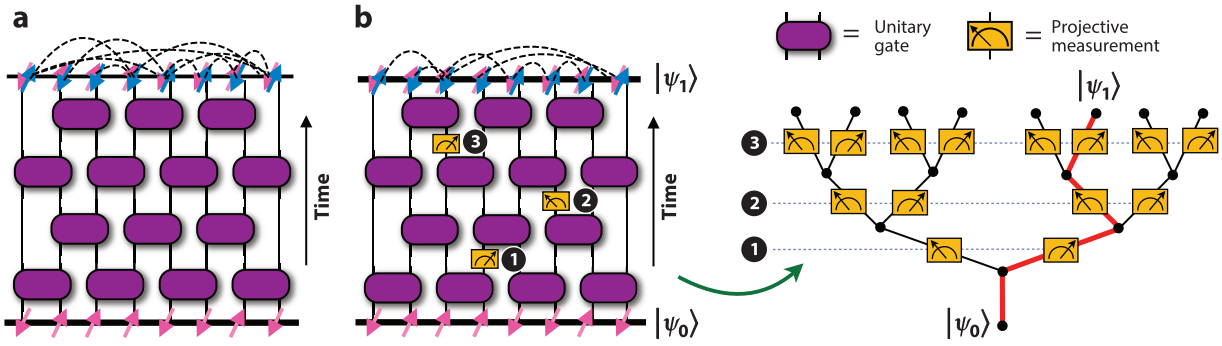

Figure 1

A space–time diagram of the two classes of quantum circuits considered in this review, with either (*a*) a brickwork structure of two-site unitary gates or (*b*) unitary gates interspersed with local projective measurements. A pure-state trajectory corresponding to a particular sequence of measurement outcomes is shown, though the inherently probabilistic nature of the measurement outcomes could yield other trajectories, which are shown schematically in panel *b*.

according to Born's rule. After an observation of the outcome $X_1 = +1$, the subsequent wave function of the two-qubit system will be given by

$$|\phi_+\rangle \equiv \frac{\mathcal{P}_+ |\phi\rangle}{\sqrt{p_+}} = \frac{1}{\sqrt{2}} [|{\rightarrow}{\rightarrow}\rangle + |{\rightarrow}{\leftarrow}\rangle] = |{\rightarrow}{\uparrow}\rangle, \qquad 7.$$

where $Z|\uparrow\rangle = |\uparrow\rangle$, so that the two qubits are now completely disentangled. Similarly, an observation of the outcome $X_1 = -1$ would have yielded the state $|\phi_-\rangle = |{\leftarrow}{\downarrow}\rangle$. As a result, after the observation of any one outcome of the measurement, the two-qubit system remains in a pure state in which the constituent qubits are disentangled from each other. In contrast, the statistical mixture of pure states obtained by averaging over both measurement outcomes with their Born probabilities,

$$\rho = \frac{1}{2} |\phi_+\rangle \langle\phi_+| + \frac{1}{2} |\phi_-\rangle \langle\phi_-| \qquad 8.$$

—which could describe the density matrix of the two-qubit system after an appropriate unitary interaction with an external bath—is a mixed state with entropy $-\mathrm{Tr}\rho\log\rho = \ln 2$, and the reduced state of each spin is maximally mixed owing to the uncertainty in the measurement outcomes.

2.3. Brickwork Random Unitary Circuit

We now turn to unitary dynamics for a chain of L qubits. In the traditional many-body setting, the starting point would be a Hamiltonian specifying evolution in continuous time. Quantum circuits (used extensively in quantum information; 40) abstract away from this and instead specify evolution in discrete time $t \in \mathbb{Z}$. For each time step there is a unitary evolution operator $U_t = U(t; t-1)$, under which a pure state (in the 2^L-dimensional many-body Hilbert space) evolves as $|\psi(t)\rangle = U_t|\psi(t-1)\rangle$. U_t is taken to be a tensor product of local unitary gates that act on pairs of spins, with the alternating structure shown in **Figure 1**:

$$U(t; 0) = U_t \ldots U_2 U_1, \qquad 9.$$

$$U_\tau = \begin{cases} \otimes_{x\in\text{odd bonds}} \; u_{\tau,x} & \text{if } \tau \text{ is odd,} \\ \otimes_{x\in\text{even bonds}} \; u_{\tau,x} & \text{if } \tau \text{ is even.} \end{cases} \qquad 10.$$

We have labeled bonds of the lattice by integers x. We leave the boundary conditions unspecified for now. Here, $u_{\tau,x}$ is a local gate, acting on the 4×4 Hilbert space for a pair of spins, which is applied (in time step τ) to the two spins connected by bond x.

Figure 1*a* can be thought of in several ways. First, it is a space–time diagram specifying which local interactions are switched on during which time steps. Second, it is also a tensor network, specifying how to build the full many-body unitary $U(t; 0)$ from four-legged tensors $u_{\tau,x}$ by contracting spin indices on all of the bonds. This contraction means summing over $\uparrow$ and $\downarrow$ on each bond (if we use, say, the Z basis). Performing this contraction, with the spin indices at the top and bottom of the circuit fixed to $\{a_1 \dots a_L\}$ and $\{b_1 \dots b_L\}$, respectively, yields the amplitude $\langle a_1 \dots a_L | U(t; 0) | b_1 \dots b_L \rangle$ to propagate between given initial and final states. Physically, the index sums make up the sum over Feynman histories of the spin chain, so, with appropriate boundary conditions at the initial and final times, a final way of viewing the circuit is as a discrete real-time path integral.

The model generalizes immediately to the case in which the local degrees of freedom are "quqits" with local Hilbert space dimension $q \geq 2$, and the local gates lie in the unitary group $\mathrm{U}(q^2)$. We start with minimally structured circuits, in which every local gate $u_{x,\tau}$ is drawn randomly and independently of all the others from the uniform distribution on the unitary group $\mathrm{U}(q^2)$. This uniform (Haar) distribution is defined by the invariance of all averages involving the random unitary $u_{x,\tau}$ under both left and right unitary rotations, $u_{x,\tau} \to v u_{x,\tau} w$, for any choices of $\mathrm{U}(q^2)$ matrices v and w. We discuss these averages (95, 96) in Section 3.

Random circuits can be used to model many kinds of dynamical process, and in many situations we choose to impose more structure or symmetry than that in the model above. (We note that even the minimal brickwork circuit above possesses one basic structure, which is spatial locality of the interactions—all-to-all-coupled circuits, in which spatial locality is relaxed, are natural in quantum information, and as toy models for black holes (23, 97–99), and we also touch on them later in the monitored setting.) In Sections 3.3.1 and 3.3.2, we review the incorporation of global symmetries (100, 101) or time-translation symmetry (102, 103) into the random circuit. Alternative choices are also possible for the distribution of unitaries or for the geometry of the circuit (in Section 3.1.2, we consider the case in which the regular brickwork of **Figure 1** is replaced with a random space–time structure). For the moment, however, we view the dynamics in a given realization of the circuit—i.e., with particular choices of the random gates $u_{\tau,x}$—as an example of a chaotic quantum evolution and compare it with more conventional nonintegrable many-body systems.

The circuit has no conservation laws (not even energy conservation). But the usual lore of local equilibration still applies. Under the evolution, an arbitrary initial state (pure or mixed) eventually equilibrates locally to the Gibbs state (2). As there are no conserved quantities here, this is simply the featureless infinite temperature state (104–106), whose entropy density $s_{\mathrm{eq}} = \ln q$ is set by the local Hilbert space dimension. The reduced density matrix of a subregion of a pure state obtains this entropy in the form of entanglement with the rest of the system, as we review in Section 3.1.

There is no notion of a ground state or of elementary excitations above a ground state. Indeed, because the circuit does not even have a discrete time-translation symmetry (except on average), the eigenstates of $U(t; 0)$ are time dependent and unlikely to be a useful starting point for computing observables. This is quite different from standard many-body systems (e.g., Fermi liquids) at asymptotically low temperature, when elementary excitations become long lived and provide a useful description of the dynamics. But the random circuits in Equation 9 (and more structured extensions of them) have proven to be useful models for various phenomena in nonintegrable dynamics at higher temperature, when the relevant timescales are much longer than the timescale for nonintegrable scattering of quasiparticles (so that quasiparticles stop being a useful language). We discuss what we can hope to study using these models in Sections 2.5 and 3.

2.4. Measurements and Trajectories

We now review some points about measurements that reappear when we discuss monitored circuits in Section 4. Measurements affect the state, and if the number of local measurements is extensive in the space–time volume, they fundamentally alter the dynamics (Section 4). The circuit is a simple setting for studying how this happens and for exploring how we should define dynamical phases and dynamical universality classes in monitored many-body systems. A basic concept is the quantum trajectory.

Imagine that an experimentalist makes a sequence of $M \geq 1$ local measurements, at various locations and times, during the circuit evolution of a pure state $|\psi\rangle$. For concreteness, let these be projective measurements of individual spins in the σ_z basis. If spin i is measured, the state undergoes the stochastic evolution,

$$|\psi\rangle \to \begin{cases} \mathcal{P}_{i\uparrow}|\psi\rangle / \sqrt{p_{i\uparrow}} \text{ with probability } p_{i\uparrow} = \langle\psi|\mathcal{P}_{i\uparrow}|\psi\rangle \\ \mathcal{P}_{i\downarrow}|\psi\rangle / \sqrt{p_{i\downarrow}} \text{ with probability } p_{i\downarrow} = \langle\psi|\mathcal{P}_{i\downarrow}|\psi\rangle, \end{cases}$$

(Born's rule), where $\mathcal{P}_{im}$ projects spin i onto $Z_i = m$.

In a given run of this experiment, the experimentalist obtains a random sequence $\mathbf{m} = (m_1, \ldots, m_M)$ of measurement outcomes, with $m_\alpha = \uparrow, \downarrow$. Note that this stochasticity should not be confused with the randomness in the unitaries. For example, we can imagine that the sequence of unitaries $\{u_{x,t}\}$ has been fixed in advance, and the experiment is repeated several times using the same unitaries. Distinct runs still yield distinct $\mathbf{m}$ in general.

A given measurement record $\mathbf{m}$, and the associated evolving state $|\psi_{\mathbf{m}}(t)\rangle$, defines a trajectory, as shown schematically in **Figure 1**. Note that, so long as our imagined experimentalist keeps a record of the measurement outcomes $\mathbf{m}$, the measurement events do not introduce any classical uncertainty about the state—it remains pure. This is unlike the interaction of an open system with a bath, where information loss to the bath forces us to work with a mixed state. [But there are formal connections between the two settings (107–109) that we discuss in Section 4.1.1.]

Another basic point is that the repeated measurements do not simply read out a preexisting unitary dynamics: They yield a new dynamics, which is a kind of random walk through Hilbert space. If our system was only a single spin, this would be a trajectory on the Bloch sphere, with measurements causing quantum jumps (107–112) to the North or South Pole (Section 2.2). In the many-body case, the problem is richer, because having local degrees of freedom means that not all points in Hilbert space are equivalent: States can be distinguished by their entanglement structure and their complexity. A local measurement disentangles spin i from all of the others. This effect competes with the spreading of correlations by the unitaries, leading to a phase transition that we review in Section 4 (53, 54, 59).

We focus on the case in which the measurements occur at a finite rate per degree of freedom. A simple choice is to let each spin be measured with probability p in a given time step, i.e., to scatter measurement events through space–time with probability p. This gives us a tuning parameter p for the strength of monitoring.

Let us formalize the monitored evolution over a time interval $[0, t]$ as a circuit. Without measurements, we would have a unitary circuit $U = U(t; 0)$. With measurements, we can define a nonunitary circuit, $K_{\mathbf{m}}$, for any given sequence of outcomes $\mathbf{m}$. This circuit is obtained from U by introducing projection operators, on bonds of the tensor network, at the space–time locations of the measurements. Repeatedly applying Born's rule shows that the probability of a trajectory $\mathbf{m}$ is $p_{\mathbf{m}} = \langle\psi(0)| K_{\mathbf{m}}^\dagger K_{\mathbf{m}} |\psi(0)\rangle$, and the final state is $|\psi_{\mathbf{m}}(t)\rangle = K_{\mathbf{m}}|\psi(0)\rangle / \sqrt{p_{\mathbf{m}}}$. It is also enlightening to study the evolution of mixed states (62): The outcome sequence $\mathbf{m}$ has probability $p_{\mathbf{m}} = \mathrm{Tr}\, K_{\mathbf{m}}\rho(0)K_{\mathbf{m}}^\dagger$ and gives the final state $\rho_{\mathbf{m}}(t) = K_{\mathbf{m}}\rho(0)K_{\mathbf{m}}^\dagger / p_{\mathbf{m}}$.

This measurement process may appear abstract. But it is a step into a rich landscape of monitored many-body quantum systems, with a wide range of different phases and phase transitions that are beginning to be explored (53, 58, 60, 61, 67, 70, 72–75, 78, 82–88, 113). The model also reveals a phase transition in the computational complexity, for a classical computer, of simulating various kinds of open or monitored quantum dynamics. Finally, it may be a toy model for certain processes in quantum information processing or encoding (57, 62, 114–117). We discuss these topics further in Section 4.

2.5. What Can We Hope to Do with These Models?

One use of the 1+1D circuits without measurements is as tractable models for nonequilibrium dynamics, thermalization, and entanglement generation in local many-body systems (17, 50, 51, 118–121). All-to-all random circuits (in which there is no notion of distance and any qubit can interact with any other) have also been used as models for scrambling in black holes (23, 97–99). In these contexts, randomness is a tool to promote solvability. Studying a specific nonintegrable model is hard. But in the random circuit it is often possible to obtain exact results for averages over the ensemble (or for typical instances). This is in the general spirit of other uses of randomness such as RMT [122; or even coding theory (123), or more recent models like the Sachdev–Ye–Kitaev model (124, 125)].

Even in the absence of conservation laws (so that there are no hydrodynamic slow modes) there are long-timescale dynamics associated with the spreading of quantum information that can be studied using the minimal random circuits above. Having a solvable model may allow us to identify coarse-grained structures that govern a broader universality class of systems. We describe examples of emergent structures in the following sections. The solvable setting also gives hints as to how to do quantitative computations in more realistic models.

If the additional symmetry of time-translation invariance is added to the circuits (102, 126), then traditional diagnostics of quantum chaos, using the eigenvalue spectrum of the time evolution operator, may be studied (Section 3.3.2). Conservation laws can be added, in order to explore the emergence of hydrodynamics (100, 101). The circuit architecture also allows structures that are not available with a fixed Hamiltonian: One can, for example, impose a duality between the space and time directions (127; Section 3.3.3) or restrict the set of allowed unitary gates so that the dynamics is classically simulable (D. Gottesman, unpublished; Section 3.3.4).

The circuits are a natural setting for adding further ingredients to the dynamics, potentially influenced by ideas from quantum computing or noisy intermediate-scale quantum devices. There is a lot of space to explore between traditional models of many-body systems (which are left to evolve with a fixed Hamiltonian) and the highly structured evolutions, with unitaries and measurements, relevant to quantum information. Random circuits are also important in quantum information as ingredients of proofs or algorithms (128) and for benchmarking (nonrandom) quantum circuits (129, 130). Because sampling the output of a sufficiently deep, random quantum circuit is believed to be prohibitively difficult for a classical computer (131), an ensemble of random circuits has recently been implemented experimentally in an attempt to demonstrate quantum supremacy (132), leading to further interest in the complexity-theoretic aspects of random circuit dynamics (129, 131, 133).

2.6. Quantum-Classical Mappings

A theme of the following is mappings between real-time quantum dynamics and effective classical statistical mechanics models. In simple limits (e.g., large local Hilbert space dimension q), some observables reduce to classical geometrical properties of the circuit (related, for example, to its

minimal cut structure or its light cone structure, as we discuss in later sections) and these limits already give some insight. But it is possible to relate the discrete path integral defined by the circuit $U = U(t; 0)$ to effective classical ensembles much more generally.

More precisely, most physical observables are expressed as multisheet path integrals (20, 134, 135), or rather multilayer circuits. Even simple expectation values such as $\langle \mathcal{O}(t) \rangle = \langle \psi(0) | U(t,0)^\dagger \mathcal{O} U(t,0) | \psi(0) \rangle$ involve the circuit and its complex conjugate: These can be represented with a doubled circuit in which U and U^* form two stacked layers. Entropies are nonlinear in the density matrix and require larger numbers of layers. A key feature of the random circuits is that these multilayer circuits simplify—only a drastically reduced set of space–time configurations survive averaging, and in simple cases the resulting configuration sum can be mapped to an effective classical partition function.

We touch on two structures. First, for small numbers of layers, circuit averages can be mapped to classical Markov processes (50, 51, 100, 118–120, 136–138), describing the incoherent (dephased) evolution of quantum operators (Sections 3.2 and 3.3.1). Second, for a general number of layers, it is possible to make a mapping to an effective classical lattice magnet, for degrees of freedom labeling pairings between layers of the circuit (Sections 3.1.3 and 4.1.2). A key role is played by domain walls in these effective magnets (50, 55, 56, 102, 103, 121, 139–143). In (1+1)-dimensions these domain walls are paths, and many basic calculations of entropies and correlators reduce to simple random walk problems. We also touch on how to generalize these ideas beyond random circuits.

3. UNITARY CIRCUIT DYNAMICS

In this section, we focus on local unitary dynamics, starting with the minimally structured case before moving on to circuits with additional symmetries or invariance properties: hydrodynamic modes (Section 3.3.1), time-translation symmetry (Section 3.3.2), space–time rotation symmetry (Section 3.3.3), or classical simulability (Section 3.3.3).

A useful way to quantify correlations in the minimally structured models of Section 2.3 is with entanglement entropies of spatial regions (and mutual information between them), because these information-theoretic quantities can be formulated without reference to any structure except locality. We start with the entanglement, which is useful for understanding the spreading of quantum information on large length scales, before discussing more conventional local correlation functions (Section 3.2). At the same time, we introduce some of the key structures underlying the analytical tractability of the circuits.

A basic point is that locality of the gates imposes a bound on the speed at which any information can spread (144). The geometry of the circuit immediately implies an upper bound of unity for this speed, but the characteristic "butterfly velocity" v_B (145, 146) for spreading of operators is typically below this geometric bound (Section 3.2). Similarly, the structure of the circuit imposes a bound on entanglement growth that is discussed in Section 3.1.2.

3.1. The Entanglement Membrane and the Pairing Order Parameter

Unitary evolution generically transforms weakly entangled pure states, which are atypical in Hilbert space (147–149), into volume-law states (12, 17, 19, 22, 150, 151). This entangling process underlies pure state thermalization and sets limits on the power of MPS and MPO simulation algorithms (94).

The entangling process is also a simple setting for introducing a basic structure underlying various calculations in random circuits, random Floquet circuits, and the monitored circuits discussed later in this review, which involves an order parameter for pairing between Feynman trajectories

in a path integral for multiple forward and backward paths (50, 52, 55, 56, 103). We discuss this in Section 3.1.3.

We start by sketching the continuum picture for entanglement production that arises from the lattice calculations (which we discuss subsequently). Random circuits lead to a coarse-grained description in which a cost is assigned to surfaces in space–time (17, 151). This theory has a broader application to chaotic systems (52, 103, 152), including holographic field theories in which remarkably explicit computations are possible (152, 153). It is also possible to discuss the entanglement of operators, as opposed to states, but we stick here to the example of entanglement generation in a state.

3.1.1. Membrane picture. Consider the growth of von Neumann entanglement entropy $S_A(t)$ of a spatial region A in an infinite d-dimensional system, after quenching from a product state. We take A to have a finite boundary area (this includes the case of a semi-infinite region in one dimension).

For generic local dynamics, entanglement is initially—i.e., on timescales that are small compared to the size of the region, though large compared to microscopic timescales—generated at a rate proportional to the area of the boundary of A (12, 20, 22, 136). If A is finite, then at asymptotically late times the thermalization of the reduced density matrix ρ_A implies that $S_A(t)$ saturates to the thermal entropy: $S_A(\infty) = s_{\rm eq}|A|$, where $|A|$ is the volume of A.

In the membrane picture (and at leading order when length and timescales are large), S_A is given by minimizing an effective free energy, or entanglement cost, for a membrane. This membrane is a d-dimensional surface lying within the $d+1$-dimensional space–time slab $t' \in [0, t]$. At the final time (top) surface $t' = t$, this membrane is anchored to the boundary ∂A between region A and its complement $\bar{A}$, and the membrane separates these two regions of the top surface, in the sense that any path from one to the other, passing through the bulk of the space–time, must intersect the membrane. At least for small enough t, the membrane spans the full time interval $[0, t]$, so it has an effective free energy that grows with t. At early times this cost is proportional to $|\partial A| \times t$, so that the initial growth of S_A is linear in t. This linear-in-time growth reflects the generation of correlations over a ballistically growing length scale (12, 19, 22). If A is finite, then at some time, proportional to the linear size of A, there is a discontinuous transition to an optimal membrane configuration that closes off in the bulk, whose cost equals the late-time entropy $S_A(\infty) = s_{\rm eq}|A|$.

The key quantity that we need to know to perform this minimization is a model-dependent "membrane tension" $\mathcal{E}(v)$. This tension depends on the local slope of the membrane with respect to the time axis, which can be parameterized with a velocity v. $\mathcal{E}(v)$ is highly constrained by causality and unitarity (note, for example, that we must reproduce the correct late-time entropy.)

The simplest case is the entanglement $S_y(t)$ of a semi-infinite region $(-\infty, y]$ in an infinite 1D chain. The membrane is then a trajectory $x_{t'}$ for $t' \in [0, t]$, with $x_t = y$, whereas x_0 is free. For a class of initial states,

$$S_y(t) = s_{\rm eq} \min \left[\int_0^t {\rm d}t' \mathcal{E}(\dot{x}) + S_{x_0}(0) \right], \tag{11.}$$

where the minimization is over trajectories respecting the final-time boundary condition $x_t = y$, and $s_{\rm eq}$ is the equilibrium entropy density ($\ln q$ in the random circuit). This may also be written as

$$\partial_t S_y = s_{\rm eq}\, \Gamma\left(\partial_y S_y\right), \tag{12.}$$

where the entanglement production rate Γ is a Legendre transform of $\mathcal{E}$.[2]

[2]We have assumed the dynamics to be homogeneous after coarse-graining as in the circuits discussed in Section 2.3 and below. Otherwise, $\mathcal{E}$ and Γ may have explicit dependence on space or time: An example is a system

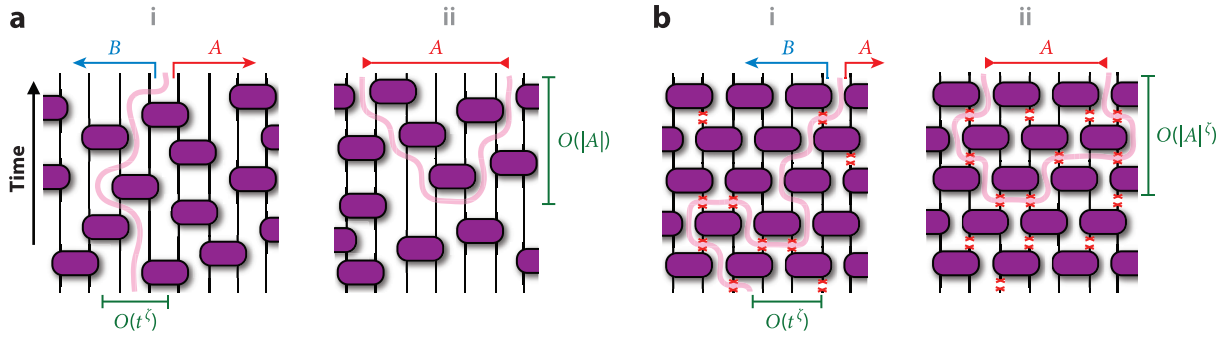

Figure 2

Minimal cuts for (*a*) unitary dynamics with geometric randomness in the applied quantum gates and (*b*) monitored dynamics, with randomly applied single-site projective measurements, which are discussed in Section 4. In panel *b*, the locations of the projective measurements are indicated by bonds with an x, which do not contribute to the cost of a minimal cut. In both kinds of dynamics, subpanel *i* shows the minimal cut corresponding to the growing entanglement of a subsystem, Whereas subpanel *ii* shows the cut corresponding to the saturated entanglement of a finite subregion. In the unitary case, the minimal cut may be taken to be strictly "causal" in the sense defined in Section 3.1.2. The transverse wandering of the minimal cut relative to its fixed endpoint(s) is governed by the wandering exponent $\zeta = 2/3$ of the directed polymer in a random environment (DPRE), as indicated in the relevant panels, which is connected with universal fluctuations of the entanglement growth (see Section 3.1.2) as well as universal subleading corrections to the entanglement entropy in the volume-law phase of the monitored dynamics (see Section 4.1.2).

For a parity-symmetric system $\mathcal{E}(v)$ is a convex function with its minimum at $v = 0$, so for a product state quench the optimal path is straight and vertical ($\dot{x} = 0$). By definition, $\mathcal{E}(0) = v_E$ gives the entanglement growth rate in this setting: $S_y(t) = s_{\mathrm{eq}} v_E t$. The line tension $\mathcal{E}(v)$ also contains information about the operator spreading velocity v_B discussed in Section 3.2, though this is in general distinct from v_E: We may argue via causality that $\mathcal{E}(v_B) = v_B$ and $\mathcal{E}'(v_B) = 1$ (151).

3.1.2. Minimal cut. The simplest version of the membrane appears in the limit $q \to \infty$, where it can be related to the idea of a minimal cut. The minimal cut is a way of bounding entanglement in any tensor network (157–161). We temporarily exchange the brickwork circuit of Section 2.3 for one with a random space–time structure: Gates are applied to bonds at random times, in a Poisson fashion, at the rate of 1 per bond. The reason for this is mentioned below. A diagram of the resulting circuit is shown in **Figure 2*a***.

When $q \to \infty$, the entanglement S_y/s_{eq} is given exactly by the cost of a minimal directed cut through this random network (17; see **Figure 2*a***). This cut is made through the bonds of the tensor network, and its cost is equal to the number of bonds cut. The cut separates the spin indices in A (at the final time boundary) from those in $\bar{A}$.

The cut is the solution to a nontrivial random optimization problem, so its exact cost depends on the circuit realization. Nevertheless, it has a well-defined deterministic line tension at large scales, telling us how many bonds we need to cut, per unit time, in order to bisect the circuit at a given angle. This is $\mathcal{E}(v) = \frac{1}{2}(1 + v^2)$ for $|v| \le 1$, and $\mathcal{E}(v) = |v|$ for $|v| \ge 1$. As a result, the entanglement growth rate in the quench from the product state is $v_E = \mathcal{E}(0) = 1/2$. The operator spreading speed may be argued to be $v_B = 1$ at large q (this is related to the average growth rate of the light cone that appears in **Figure 2*a***, subpanel *ii*), so the constraints above,

with spatial "weak links" (154). In general, $\mathcal{E}$ will also depend on any hydrodynamic densities that are present and on a thermodynamic entropy current if conservation laws allow one (153, 155, 156).

$\mathcal{E}(v_B) = v_B$ and $\mathcal{E}'(v_B) = 1$, are satisfied. The entanglement production rate Γ in Equation 12 is $\Gamma(s) = \frac{1}{2}[1 - (s/s_{\rm eq})^2]$, so that $\partial_t S$ is largest when $\partial_x S$ is zero.

The line tension $\mathcal{E}(v)$ sets the leading, deterministic growth of $S_y(t)$ at large t. This picture also reveals subleading structure arising from randomness in the circuit. At the moment, this randomness is the geometrical randomness in the circuit, but we see below that randomness in the unitaries has a similar effect, even in the geometrically regular brickwork circuit, when q is finite.

Finding the optimal cut is a version of the directed polymer in a random environment (DPRE) problem, with nontrivial critical exponents (162, 163). In the quench from the product state, $S_y(t)$ has the Kardar–Parisi–Zhang (KPZ) scaling $S_y(t) = s_{\rm eq}(v_E t + bt^{1/3}\chi_{y,t})$. The exponent 1/3 of the subleading term is universal. $\chi_{y,t}$ is a random variable, of order 1 size, that depends on the realization (164–166).

These fluctuations may also be understood in the language of Equation 12, which, after including subleading terms, including noise, and expanding Γ to quadratic order, becomes the KPZ stochastic equation for the entropy profile $S_y(t)$.

The minimal cut also describes the saturation of the entanglement entropy of a finite region at late times. In (1+1)-dimensions, the entanglement of a region of finite width ℓ (in an infinite system) grows until a time $t_\star = \ell/2v_E$, at which point the entanglement of the region reaches its maximum value $S_\ell(t > t_\star) = s_{\rm eq}\ell$. At times $t < t_\star$, the minimal cut for $S_\ell(t)$ consists of two curves, one for each endpoint of the region, which are vertical (oriented in the time direction). At times $t > t_\star$, the minimal cut consists of a single curve connecting the two endpoints of the region that intersects ℓ bonds of the circuit. This curve is not unique, but it can be chosen to be oriented along the light cone of the quantum circuit as in **Figure 2*a***. In the formalism of Section 3.1.3, the analogous membrane has a definite coarse-grained V shape, made up of two segments that travel at speed $\pm v_B$.

The minimal cut is an exact description of the entanglement entropy only when $q = \infty$. However, many aspects of the phenomenology survive at finite q. Next, we discuss a more generic approach to deriving the membrane.

3.1.3. The pairing order parameter. The Rényi entropies are examples of observables that can be expressed in terms of multilayer circuits, built by stacking copies of $U(t)$ and $U(t)^*$ and attaching appropriate boundary conditions to the initial and final-time bonds: The nth Rényi entropy involves n copies each of $U(t)$ and $U(t)^*$, as discussed below for the example of S_2.

Formally, such a stack describes unitary evolution going on in parallel in several copies of the spin chain. This evolution may be formulated in terms of Feynman trajectories for each copy (the sum over trajectories is equivalent to the contraction of the tensor network; see Section 2.3). A key quantity in this setting is an order parameter labeling pairing between Feynman trajectories (50–52, 103, 121, 142). Heuristically, phase cancellation is avoided if the trajectory for each forward [i.e., $U(t)$] layer is locally similar to that for a paired backward [i.e., $U(t)^*$] layer, and there are several ways to choose the pattern of pairing. This intuition can be made precise in the brickwork circuit of Section 2.3.

The Rényi entropies are nonlinear functions of the density matrix; e.g., the second Rényi entropy S_{2A} is given by (Section 2.1)

$$\exp[-S_{2A}(t)] = {\rm Tr}_A\, \rho_A(t)^2, \qquad \text{with } \rho_A(t) = {\rm Tr}_B\, \rho(t). \tag{13.}$$

Again, consider a quench from a product state. As a tensor network, the evolving state $|\psi(t)\rangle$ is expressed using a single copy of the circuit (with product states attached to the bonds at the bottom, and the bonds at the top being the wave function's spin indices). The density matrix $\rho(t) = |\psi(t)\rangle\langle\psi(t)|$ involves the bra and the ket, so it can be represented as a two-layer circuit,

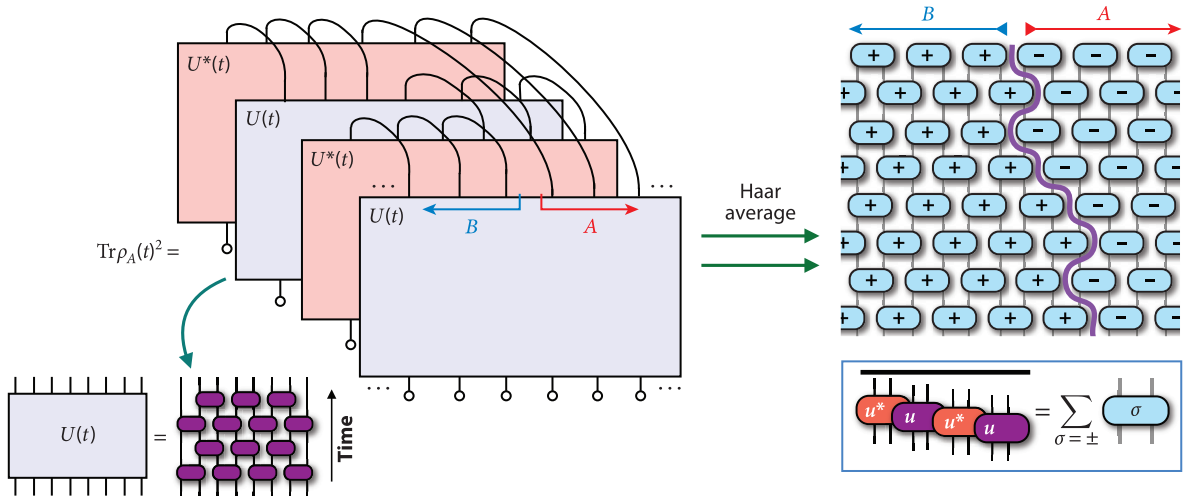

Figure 3

Performing an average over the Haar measure, for each local unitary gate in the brickwork quantum circuit, transforms $\mathrm{Tr}\rho_A(t)^2$ into the partition function of a type of 2D classical Ising model, with a single Ising spin for each two-site quantum gate.

where the bra layer is complex conjugated. The quantity $\mathrm{Tr}\,\rho_A(t)^2$, known as the purity of region A, is thus a four-layer circuit, with two backward (complex conjugated) and two forward layers. As a result of the traces in Equation 13, these layers are sewn together at the final time boundary in the manner shown in **Figure 3**. This is a discrete version of a path integral with two backward and two forward trajectories. Let us label the forward layers 1 and 2 and the backward layers $\bar{1}$ and $\bar{2}$.

This structure describes time evolution going on in parallel in four "universes," one for each copy of the circuit. Correspondingly, there is now in total a q^4-dimensional Hilbert space associated with each spatial position, and each physical gate yields a replicated gate $u \otimes u^* \otimes u \otimes u^*$ in the multilayer circuit, where u^* is complex-conjugated in the computational basis. However, if we consider the average over random unitaries, $\overline{\mathrm{Tr}\,\rho_A(t)^2}$, there is a remarkable simplification. The average can be performed separately for each local gate u because these are independently random. (In the following, we are schematic; see (50, 52) for more careful exposition of the effective lattice model.)

For simplicity, consider a single-site rather than a two-site gate (this does not change the basic point). The Haar average of $u \otimes u^* \otimes u \otimes u^*$ is a projection operator onto the subspace of the q^4-dimensional Hilbert space that is invariant under $u \otimes u^* \otimes u \otimes u^*$ for every u (167). This is spanned by only two states, denoted $\|+\rangle\rangle$ and $\|-\rangle\rangle$. Schematically,

$$\overline{u \otimes u^* \otimes u \otimes u^*} = P_+ + P_- = \sum\nolimits_{\sigma=\pm} P_\sigma. \qquad 14.$$

This decomposition involves nonorthogonal projectors onto $\|+\rangle\rangle$ and $\|-\rangle\rangle$.

The states $\|+\rangle\rangle$ and $\|-\rangle\rangle$ have a simple physical interpretation. Formally, they are obtained by pairing up the four layers in one of two possible ways illustrated below, and forming a maximally entangled state for each pair, in the following pattern:

$$+ : \quad \overline{1}\,\overline{1}\,2\,\overline{2}, \qquad\qquad - : \quad \overline{1}\,2\,\overline{1}\,\overline{2}. \qquad 15.$$

The states in Equation 15 generalize the simpler version for just two copies that we denote $\|\mathbb{1}\rangle\rangle$ as

$$\mathbb{1} : \quad \overline{1}\,\overline{1}. \qquad 16.$$

In components, $\mathbb{1}_{ab} = \delta_{ab}$, and analogously for the states in Equation 15 with more layers. The invariance $(u \otimes u^*)\,\|\mathbb{1}\rangle\rangle = \|\mathbb{1}\rangle\rangle$ is easily checked to be a restatement of the unitarity of u.

The above is for a single gate acting on one site: When we perform a similar average over all the gates in the circuit, we project the dynamics into the space spanned by locally paired states, with the local choice of pairing possibly varying throughout space. In the language of Feynman trajectories, paired trajectories survive the average because the layers within a pair contribute equal and opposite phases to the path integral.

Concretely, Equation 14 means we can trade the unitary average for a sum over an Ising-like degree of freedom $\sigma = \pm$. Doing this for every gate in the brickwork circuit of **Figure 3** maps $\mathrm{Tr}_A\, \rho_A(t)^2$ to the partition function of a 2D classical Ising-like model, with one Ising spin for each physical gate. The Boltzmann weight of this Ising model, for a given σ configuration, is obtained by contracting a tensor network made up of two-site projection operators, which yields local interactions for the σ spins. These interactions are anisotropic and encode hard constraints on the spin configuration that ensure observables are consistent with the underlying unitarity of the dynamics. For example, as we proceed downward, it is impossible to nucleate a domain of $-$ inside a uniform domain of $+$, and vice-versa.

Generalizations of these pairing of degrees of freedom are important for random unitary circuits (50, 121), random tensor networks (RTNs; 139, 141), random Floquet circuits (103), and monitored circuits (55, 56, 58, 88) and can even be defined in nonrandom circuits (52). Here, the structure imposed by unitarity radically simplifies the resulting Ising model. In the present setting, taking A and $\bar{A}$ to be the two semi-infinite halves of the chain, $\overline{e^{-S_{2A}}}$ becomes a partition function for Ising configurations with a single directed domain wall, as illustrated in **Figure 3**. This domain wall is reminiscent of the minimal cut discussed above, but in addition to an energy it has a nontrivial entropy associated with thermal fluctuations in the effective model. If $q \to \infty$, then the energy term dominates, and this reproduces the minimal cut result. For $q < \infty$, both energy and entropy contribute to a coarse-grained line tension $\mathcal{E}(v)$ that can be easily computed.[3]

The averaged purity is only a starting point. First, in the random circuit, we would really like to compute $\overline{S_{2A}}$ rather than $\overline{e^{-S_{2A}}}$, because the exponential average can be dominated by rare realizations. Second, we would like to use the structure above as a guide to calculations in more general models, perhaps without randomness.

In the random case, $\overline{S_{2A}}$ can be obtained by extending the above calculation using the replica trick (121) that also plays an important role in RTNs (141). Here, we give another viewpoint (52), which also extends to circuits without any randomness.

Consider a particular circuit instance—e.g., a particular realization of the random unitaries. Then, for a given gate u in the circuit, we may write the tautology,

$$u \otimes u^* \otimes u \otimes u^* = P_+ + P_- + R^u_\perp. \qquad 17.$$

Comparing to Equation 14, $R^u_\perp$ is a remainder left over when $u \otimes u^* \otimes u \otimes u^*$ is projected to the nonpaired subspace. Using this representation for every gate, $e^{-S_{2A}}$ is formally equal to the partition function of a generalized Ising model in which the spins take values $+, -, \perp$. (The spin configurations are again constrained as a result of the underlying unitarity.)

[3]Note that in the brickwork circuit the shape of the minimal cut is highly degenerate. This is why we instead used the randomly structured circuit to discuss the $q = \infty$ limit. The degeneracy in the brickwork circuit corresponds to $\mathcal{E}(v)$ becoming a trivial v-independent constant (for $|v| < 1$) in the limit $q \to \infty$. However, once q is finite, $\mathcal{E}(v)$ is nontrivial, so the degeneracy is resolved for the coarse-grained entanglement membrane. Dual-unitary circuits are a class of systems in which $\mathcal{E}(v)$ is flat even at finite q (52, 168).

The weights of configuration with only + and − are the same as before, but local clusters of ⊥ spins have a nontrivial weight that depends on the local unitaries. At first sight this looks complicated, but a simple picture is recovered after coarse-graining. We still have a domain wall between + and −, but it is dressed on microscopic scales by insertions of ⊥ along its length. This is particularly simple at large but finite q, when ⊥ spins can be shown to be very dilute. They can be explicitly integrated out, giving a renormalization (of order q^{-2}) of the local domain wall cost.

This renormalization has two effects. First, it slightly renormalizes the membrane tension $\mathcal{E}(v)$: This reflects the difference between averaging S_2 and averaging its exponential. Second, it means that the local cost of the domain wall varies from place to place in the random circuit because $R^u_\perp$ in Equation 17 depends on the local random gate. This amounts to a random local potential for the polymer. Although the microscopic picture is rather different from the minimal-cut-in-a-random-environment in Section 3.1.2, we obtain the same universal physics at large length scales: S_{2A} maps to the free energy of a DPRE with its characteristic exponents.[4]

We may also consider the case in which the circuit is translationally invariant. Equation 17 allows a nonrandom system to be treated by a kind of perturbation theory around the random circuit result, taking into account successively larger clusters of ⊥ (52). This is a way to derive the membrane beyond the random circuit context.

The pairing structure in Equations 14 and 15 generalizes to an arbitrary number of layers and can be used to discuss the entanglement entropies with integer Rényi index $n > 1$ (or higher moments of the purity, as required for the replica trick) and many other quantities.

In the general case with N layers each of $U(t)$ and $U(t)^*$, the spin σ labeling different patterns of pairing becomes an element of the permutation group, $\sigma \in S_N$ (121, 139, 141). The effective statistical mechanics problem has a symmetry that is in general (52, 121, 141, 169)

$$G_N \equiv (S_N \times S_N) \rtimes \mathbb{Z}_2, \qquad 18.$$

where the two copies of S_N (acting as $\sigma \to g_F \sigma g_B^{-1}$ for $g_F \in S_N, g_B \in S_N$) arise from symmetry under permutations of the forward and backward layers, respectively, and the $\mathbb{Z}_2$ generator is associated with exchange of forward with backward layers and acts as $\sigma \to \sigma^{-1}$.

Domain walls have an interesting combinatorial structure for $N > 2$: Each domain wall is labeled by a permutation group element, and domain walls can split and recombine in accordance with the rules for composing permutations (88, 103, 121, 141).[5] We return to these domain walls in Section 4.1.2.

Let us comment on the special case of the von Neumann entropy. In the approach sketched around Equation 17, the entanglement membrane has a clear meaning—as a domain wall in a well-defined degree of freedom σ—for the Rényi entropies S_n with $n > 1$. The von Neumann entropy S_1 is more subtle, and in the current approach must be treated via an analytic continuation (e.g., of S_n for $n > 1$). Because this continuation is difficult, and because S_1 has a special status among the Rényi entropies,[6] it would be desirable to have a more direct construction of the entanglement

[4]The minimal cut problem is a zero temperature problem involving only energy minimization, whereas the domain wall above is effectively at finite temperature. However, temperature is an irrelevant perturbation for the DPRE, so this difference does not change the basic exponents.

[5]The N-dependent domain wall structure means that distinct Rényi entropies have distinct line tensions $\mathcal{E}_n(v)$ in general. At late times, it also explains the Page subleading correction to S_{nA} in the case in which A contains half the total number L of qubits, $S_{nA} = s_{\rm eq}(L/2) - (n-1)^{-1} \ln C_n$, where C_n is the nth Catalan number: In the domain wall picture, $\ln C_n$ is an entropic factor from counting the number of energetically equivalent domain wall configurations.

[6]For example, the higher Rényi entropies can fail to be the most natural measures for entanglement in some settings, such as many models with conservation laws (170–174), where $S_{n>1}$ grows parametrically slower than S_1.

membrane for S_1. Apart from the limit of infinite q mentioned above, direct calculations of the von Neumann entropy have so far been possible only for circuits with special structure such as dual unitarity (168; Section 3.3.3) or Clifford (17, 51; Section 3.3.4). Exact computations of the von Neumann entropy are possible in a completely different kind of large N limit, using holography and the Hubeny–Ryu–Takayanagi (HRT) prescription for entanglement, in terms of a surface in a higher-dimensional Anti–de Sitter space (22, 27, 150, 175). In the appropriate scaling limit, these results are consistent with the membrane picture above (152, 153).

3.2. Spreading and Decay of Correlations

The evolution of local observables also exhibits universal structure, for example in the decay of correlations and in the process of scrambling, where information that is initially stored locally becomes delocalized (176–178). Circuits give an intuitive picture for these processes in terms of Feynman trajectories of operators $\mathcal{O}(t)$.

For an L-site spin-1/2 system evolved by the quantum circuit $U(t) = U_t U_{t-1} \cdots U_1$, define the evolution of a local Pauli operator $\mathcal{O}(\boldsymbol{r}, 0)$ as $\mathcal{O}(\boldsymbol{r}, t) = U(t)\mathcal{O}(\boldsymbol{r}, 0)U(t)^\dagger$—for convenience, we use the reverse of the usual Heisenberg picture convention here. Scrambling requires the increase in complexity and spatial extent of $\mathcal{O}(\boldsymbol{r}, t)$ with time: If, say, information is initially stored in the eigenvalue σ of the local operator, $\mathcal{O}(\boldsymbol{r}, 0)\,|\psi\rangle = \sigma\,|\psi\rangle$, then at later times this information is stored via the evolved operator, $\mathcal{O}(\boldsymbol{r}, t)|\psi(t)\rangle = \sigma|\psi(t)\rangle$, which has become delocalized in its support.

This operator may be expanded as a superposition of strings $\mathcal{S}$, each of which is a product of Pauli matrices at distinct lattice sites, so that (13, 24)

$$\mathcal{O}(\boldsymbol{r}, t) = \sum_{\mathcal{S}} a_{\mathcal{S}}(t)\mathcal{S}. \tag{19.}$$

The string operators satisfy $\mathrm{Tr}(\mathcal{S}\mathcal{S}') = \delta_{\mathcal{S}\mathcal{S}'}$ (the trace Tr is normalized so $\mathrm{Tr}\,\mathbb{1} = 1$) and the Pauli operator $\mathcal{O}$ obeys $\mathrm{Tr}[\mathcal{O}(\boldsymbol{r}, t)^2] = 1$. Therefore, the coefficients satisfy

$$\sum_{\mathcal{S}} a_{\mathcal{S}}(t)^2 = 1, \tag{20.}$$

so that $a_{\mathcal{S}}(t)$ may be viewed as the amplitudes for an evolving, quantum mechanical "operator wave function" in a 4^L-dimensional Hilbert space (each site can be $\mathbb{1}$—i.e., not part of the string—or X, Y, or Z; 50, 51).

The evolution $\mathcal{O}(\boldsymbol{r}, t+1) = U_{t+1}\mathcal{O}(\boldsymbol{r}, t)U_{t+1}^\dagger$ is a linear, unitary evolution of this operator wave function, $a_{\mathcal{S}}(t+1) = \sum_{\mathcal{S}'} W_{\mathcal{S}\mathcal{S}'}(t)a_{\mathcal{S}'}(t)$, with the matrix $W_{\mathcal{S}\mathcal{S}'}(t) \equiv \mathrm{Tr}(U_{t+1}\,\mathcal{S}\,U_{t+1}^\dagger\mathcal{S}')$. This operator dynamics simplifies for the circuit composed of Haar random unitary gates $u_{x,t}$ (Section 2.3). In that case, taking the Haar average over the gates $u_{x,t}$ gives

$$\overline{W_{\mathcal{R}\mathcal{R}'}(t)\;W_{\mathcal{S}\mathcal{S}'}(t)} = \delta_{\mathcal{R},\mathcal{S}}\,\delta_{\mathcal{R}',\mathcal{S}'}\,T_{\mathcal{S}\mathcal{S}'}(t). \tag{21.}$$

The transfer matrix $T_{\mathcal{S}\mathcal{S}'}(t)$ defines a Markov process on the space of basis operators, with local updates of the strings and string probabilities $a_{\mathcal{S}}^2$ (50, 51, 118, 119, 136, 137):

$$\overline{a_{\mathcal{S}}(t+1)^2} = \sum_{\mathcal{S}'} T_{\mathcal{S}\mathcal{S}'}(t)\overline{a_{\mathcal{S}'}(t)^2}. \tag{22.}$$

For the initially local operator, this process can be mapped to a classical cluster growth process with an effective stochastic dynamics for the boundaries of the operator (50, 51). The initial string is supported on one site, e.g., $\mathcal{O}(\boldsymbol{r}, 0) = Z_{\boldsymbol{r}}$. This site forms the seed for a cluster of Pauli operators that grows with time (in order to exploit the entropy of the cluster in the classical model). The boundaries undergo their own effective stochastic dynamics, which in (1+1)-dimensions is just biased diffusion.

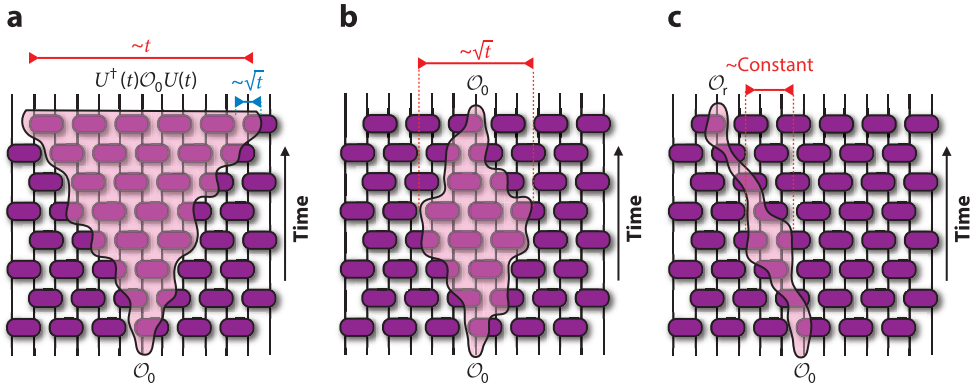

Figure 4

The typical support of an initially local operator grows ballistically under Heisenberg evolution by a minimally structured unitary quantum circuit, whereas (*a*) the width of the operator's front broadens diffusively in (1+1)-dimensions. Atypical operator Feynman trajectories contribute to time-ordered correlations of local observables. (*b*,*c*) Two different classes of atypical trajectories can provide dominant contributions to the mean-squared correlator.

In (1+1)-dimensions, the two boundaries of the cluster move outward ballistically with butterfly velocities, $\pm v_B$; in the limit that the on-site Hilbert space dimension $q \to \infty$, v_B approaches the maximum (light cone) speed $v = 1$ of the quantum circuit, whereas $v_B < 1$ when q is finite (e.g., for spin-1/2 degrees of freedom). The growth of an initially local operator can be measured with the out-of-time-order correlation (OTOC) function $-\frac{1}{2}\overline{\mathrm{Tr}([\mathcal{O}(\boldsymbol{r},t),\mathcal{O}(0,0)]^2)}$ that saturates to 1 for $|r| \lesssim v_B t$ and is exponentially small for $|r| - v_B t \gg 1$. The OTOC has been used to diagnose the scrambling of locally accessible quantum information (176–178), and its growth in time provides signatures of key properties of quantum many-body systems, including their chaotic (135, 179–181), disordered (154, 182–187), or integrable (188–191) nature. OTOCs have been addressed in a range of experiments (113, 192–195).

In (1+1)-dimensions, the Markov process on strings simplifies substantially, giving rise to a Markov process for the left and right endpoints of an operator string, which perform biased random walks. Their stochastic fluctuations set the scale on which the plateau in the OTOC is rounded, so that the edge of the operator broadens diffusively as $t^{1/2}$ in (1+1)-dimensions. In (d+1)-dimensions with $d > 1$, operator growth is governed by a Markov process for a d-dimensional cluster. In the simplest case, the stochastic growth of the edge of this cluster is in the universality class of the KPZ equation for a (d−1)-dimensional interface, which grows ballistically and broadens in time as t^β, where $\beta = 1/3$ in $d = 2$ spatial dimensions (163).

In (1+1)-dimensions, typical operator trajectories look like **Figure 4*a***. By contrast, time-ordered correlators such as $G(\boldsymbol{r},t) \equiv \mathrm{Tr}[\mathcal{O}(\boldsymbol{r},t)\mathcal{O}(0,0)]$ are determined by atypical operator trajectories and look quite different (196). Instead of growing ballistically, the string is small at the final time as in **Figure 4*b*,*c***. The nonvanishing average $\overline{G(r,t)^2}$ defines a sum over space–time paths taken by the operator endpoints, which start at the origin and end at position $\boldsymbol{r}$ at time t. The atypical trajectories of the endpoints that are required by these boundary conditions give rise to exponential relaxation, $\overline{G(vt,t)^2} \sim \exp[-r(v)t]$, as expected for a model without slow modes. Physically, this demonstrates that local degrees of freedom are decohered on an order-1 timescale by the other degrees of freedom, which act as a bath.

However, there is nontrivial structure in the decay rate $r(v)$ (196). In the 1+1D Haar circuit, the dominant contribution to the correlation function changes from trajectories of the endpoints,

which are (*a*) bound together when $v > v_B$ to (*b*) unbound when $v < v_B$. This unbinding phase transition may be detected in a nonanalyticity of the decay rate $r(v)$ as a function of velocity.

The fact that correlators are dominated by operator trajectories that are more spatially compact than the support of operator is generic. It can also be observed in dual-unitary circuits (197), and it implies that numerical evaluation of such correlators using the Heisenberg picture is more efficient than ballistic operator growth would suggest (198, 199).

3.3. Structured Unitary Circuits

The preceding sections illustrate how minimally structured random circuits help to uncover universal properties of quantum dynamics that follow from unitarity and locality alone. However, many physically relevant models (such as time-independent Hamiltonians) have additional structures that must enter a universal description of the dynamics, for instance, hydrodynamic modes associated with conserved densities. We now discuss examples of more structured quantum circuits that nevertheless retain analytic tractability.

3.3.1. Circuits with continuous symmetries. Random circuits can be enriched with continuous global symmetries; for instance, they can be constrained to obey a U(1) conservation law for total charge. Khemani et al. (100) and Rakovszky et al. (101) studied such a model and obtained an emergent classical description of slow diffusive modes associated with the conserved densities. These slow modes lead to power-law hydrodynamic late-time tails in both time-ordered and out-of-time-ordered correlators. In addition, Khemani et al. (100) described the interplay between the slow modes and the other (fast) degrees of freedom to furnish a microscopic derivation of how (reversible) unitary dynamics can give rise to diffusive (dissipative) hydrodynamics. This addresses a long-standing question in quantum statistical mechanics, namely of reconciling hydrodynamics—which is a dissipative classical theory for a few coarse-grained degrees of freedom—with linear, unitary quantum time evolution on an exponentially large Hilbert space.

Quantum circuits, by definition, are discrete time evolutions and, hence, cannot conserve energy that requires continuous time-translation symmetry. Instead, the system can be made to conserve a total charge, for instance, total $S^z_{\text{tot}} = \sum_i Z_i$. Each gate conserves S^z locally and, so, has a block-diagonal structure, with each block (acting within a particular charge sector) being an independent Haar random unitary. The conservation law induces nonlinearities in the equations for the weights $\overline{a_S^2}$ (the analog of Equation 22) but analytical tractability is retained in a type of large-q limit, in which each site hosts both the qubit whose z component is conserved and an unconstrained large-q degree of freedom (100).

A local charge density operator at the origin, $Z_0(t) = \sum_{\mathcal{S}} a_S(t)\mathcal{S}$, can again be expanded in a basis of Pauli operators. In addition to the normalization constraint (Equation 20) on the 4^L weights $a_S(t)^2$, the conservation of S^z_{tot} requires normalization of the L amplitudes of the local conserved densities, Z_i, in the operator expansion of $Z_0(t)$:

$$\sum_i a_{Z_i}(t) = 1, \qquad 23.$$

which follows from $\text{Tr}[Z_0(t)S^z_{\text{tot}}] = \sum_i a_{Z_i}(t) = \text{Tr}[Z_0 S^z_{\text{tot}}] = 1$. After Haar averaging, the effect of a gate acting on sites x and $x+1$ is to spread charge uniformly between these sites[7]:

$$\overline{a_{Z_x}(t+1)} = \overline{a_{Z_{x+1}}(t+1)} = \frac{\overline{a_{Z_x}(t)} + \overline{a_{Z_{x+1}}(t)}}{2}. \qquad 24.$$

[7]Note that the amplitudes of conserved densities survive Haar averaging in a U(1) symmetric system, whereas only the weights survive averaging in a Haar random circuit with no symmetries.

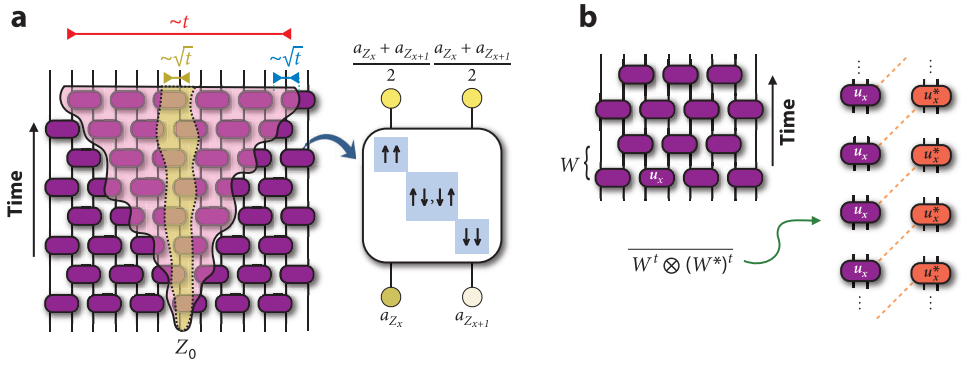

Figure 5

The spreading of the local charge density $Z_0(t)$ by a quantum circuit that conserves $S^z_{\text{tot}} \equiv \sum_i Z_i$ is shown schematically in panel *a*. As described in Section 3.3.1, the region of support of this operator grows ballistically while retaining a weight on a diffusive lump of conserved charges near the origin. A Floquet circuit composed of Haar random unitary gates is shown in panel *b*. Averaging over this ensemble in the calculation of the spectral form factor leads to a pairing degree of freedom for each unitary gate in a Floquet period, which simplifies in the limit of large local Hilbert space dimension $q \to \infty$, as described in Section 3.3.2. One of the possible pairings in this limit is indicated by the dashed lines in panel *b*.

Upon coarse-graining, Equation 24 becomes a diffusion equation for the conserved quantity a_{Z_i}, with diffusion constant $D = 1/2$. This implies that the relaxation of the conserved density is diffusive, as expected:

$$\text{Tr}[Z_0(t)Z_x] = a_{Z_x}(t) = \frac{1}{\sqrt{2\pi t}} e^{-\frac{x^2}{2t}}.$$

The total operator weight $\sum_{\mathcal{S}} a_{\mathcal{S}}^2 = w^{\text{c}} + w^{\text{nc}}$ may be decomposed into a part w^{c} supported on the U(1) conserved densities Z_x, and a part w^{nc} supported on more general strings, with $w^{\text{c}} + w^{\text{nc}} = 1$. Although the sum of conserved amplitudes is constant, the weight w^c on the densities decreases as a power law: $\overline{w^{\text{c}}(t)} = \frac{1}{2\sqrt{\pi t}}$. This is due to local conversion of conserved to nonconserved operators, at a rate proportional to the square of the local conserved current. The emitted nonconserved parts then grow at the butterfly speed, as before. This process can be described via coupled hydrodynamic equations (100).

The spreading operator has a characteristic shape that can be detected with the OTOC. The front remains ballistic, but the slow conversion of conserved to nonconserved operators leads to a diffusing lump of local conserved charges near the origin, as shown schematically in **Figure 5*a***, and also to power-law tails behind the front: These are due to lagging fronts of nonconserved operators that are emitted at later times during the operator's evolution.

Physically, the emission of long strings allows physical observers to see a decay of correlations and an increase in observable entropy even though, by unitarity, the von Neumann entropy of the full system remains unchanged. This is really a decay of correlations detectable with simple operators, due to the hiding of correlations in highly nonlocal operators.

The case of U(1) symmetric diffusive circuits has been generalized to more exotic variants. For instance, higher-dimensional circuits with subsystem symmetries acting on lower-dimensional submanifolds can lead to anomalous subdiffusive dynamics (200). A separate line of work studied fractonic circuits that conserve both a U(1) charge, $Q = \sum_x q_x$, and its dipole moment, $P = \sum_x x q_x$ (201–205), or even higher multipole moments (206). This is found to lead to a novel form of ergodicity breaking via the shattering of Hilbert space into exponentially many dynamically decoupled sectors, with no dynamical path even between states with the same charge and dipole quantum

numbers (203, 204)—which is a surprising result in light of the conventional belief that ergodicity breaking requires extensively many conservation laws, as in integrable systems.

Before leaving this section, we comment briefly on implications of results derived for noisy (random in time) quantum circuits for deterministic dynamics. The broad features discussed here, for instance, regarding the behavior of OTOCs and entanglement in systems with and without conservation laws, have numerically been verified to also hold more generally for deterministic dynamics generated by thermalizing time-independent Hamiltonians or time-periodic Floquet circuits. [A caveat is that in the presence of conservation laws, the higher Rényi entropies can be anomalously affected by rare events in which the local charge is highly depleted, so that they grow and spread more slowly than the von Neumann entropy (170–174).] One heuristic picture is that thermalizing systems can act as their own bath and generate a noisy environment for subsystems (207). Alternately, as discussed in Section 3.1.3, the effective degrees of freedom that can be identified microscopically in the random circuit also emerge after coarse-graining in more general models.

3.3.2. Floquet circuits. An important class of structured circuits possesses discrete time-translation symmetry. If in the brickwork circuit (Section 2.3) the first two layers of gates are repeated periodically, then $U(2t; 0) = W^t$, where the evolution operator for one period is $W = U_2 U_1$. Any initial state can be expanded in the eigenbasis of W, so that the spectrum of W plays a similar role to that of a time-independent Hamiltonian for continuous time evolution.

A large class of chaotic many-body Floquet systems without conservation laws thermalize to infinite temperature, like the fully random circuits discussed in Section 2.3. Although we focus here on chaotic Floquet dynamics, it should be noted that random Floquet circuits can also exhibit MBL (102, 208–212). In particular, Reference 208 emphasized the quantum circuit language, constructing a random Floquet circuit of Clifford gates (Section 3.3.4) that showed a solvable localization transition, related to classical percolation of spatial puddles. For localized Floquet dynamics, the system can avoid thermalizing to infinite temperature, allowing for novel dynamical phases such as the Floquet time crystal phase, which spontaneously breaks discrete time-translation symmetry (213, 214), and in two dimensions the anomalous Floquet insulator, with protected chiral edge modes (215–217).

We turn now to a headline result in the study of chaotic Floquet quantum circuits, which is a demonstration of the random matrix spectral statistics that are often taken as a practical definition of quantum chaos. There is a plethora of numerical evidence that spectral correlations in chaotic many-body systems are universally described by RMT (1, 218), but an explicit derivation away from a semiclassical single-particle limit has been a longstanding open problem. This has been achieved in both Haar random brickwork Floquet circuits in the limit of large local Hilbert space dimension q (below; 102, 103)—see also Reference 126 in a slightly different setting—and in certain dual-unitary Floquet circuits with no large parameters (219–221; see Section 3.3.3). Themes discussed in previous sections, including the pairing of Feynman trajectories and the mapping of circuits to effective classical statistical models, feature centrally in both results.

Within RMT, a standard probe of correlations between the eigenvalues $\{e^{i\theta_n}\}$ of W is the spectral form factor (SFF), which is defined as

$$K(t) = \left|\mathrm{Tr}\, W^t\right|^2 = \sum_{m,n} e^{i(\theta_n - \theta_m)t}. \qquad 25.$$

If W is a Haar random unitary acting on the full Hilbert space of L qudits, each with Hilbert space dimension q, then the SFF averaged over this ensemble is $\overline{K_{\mathrm{Haar}}(t)} = t$ for $1 \le t \le q^L$. This linear growth (ramp) in the SFF characterizes the level repulsion between pairs of eigenvalues across the entire eigenspectrum within RMT (222). Generalizations of the SFF (Equation 25)

have also been introduced in order to uncover the precise sense in which RMT can describe the far-from-equilibrium dynamics of a quantum many-body system (223, 224).

Turning to the case in which W describes a quantum circuit composed of local unitary gates, $K(t)$ becomes a two-layer circuit with periodic boundary conditions in the time direction and can be written as a double sum over periodic Feynman trajectories, one in each layer. Terms in which the forward and backward trajectories are equal up to a time translation are special, in that their phases cancel and they give a positive contribution to the sum. Heuristically, the behavior $\overline{K(t)} = t$ arises from the fact that there are t ways in which the forward trajectory can be translated with respect to the backward trajectory. Pairings of trajectories that are not related by a time translation can contribute any phase to the SFF, and within a given Floquet dynamics, the large number of such pairings can combine to provide a contribution to the SFF that is of the same order as the ramp. As a result, the SFF is not a self-averaging quantity (225). Averaging the SFF over a time window, or over an appropriate ensemble of Floquet dynamics, is required in order to eliminate these contributions.

This understanding can be made concrete in random Floquet circuits in (1+1)-dimensions (102, 103, 226). Averaging over the Haar random gates in this setting gives a sum over diagrams involving pairings between the layers. In general these may be extremely complicated, but in the limit $q \to \infty$ there is a great simplification. The diagrams can be represented as pairings between the gates of the forward and backward layer, and only t diagrams survive (102, 103), which are labeled by a time shift $s \in \{0, \ldots, t-1\}$: A given unitary $u_{x,\tau}$ in the forward layer is paired with $u^*_{x,\tau+s}$ in the backward layer. An example of such a pairing is shown in **Figure 5*b***. For a fixed system size L and at sufficiently long times, the pairing degrees of freedom for each Haar random unitary gate in W are forced to be identical (103, 226, 227). Summation over the t possible choices recovers the RMT behavior $\overline{K(t)} = t$.

A modified $q \to \infty$ model contains nontrivial finite-time corrections to the SFF (102). In this model, the SFF maps to the partition sum for a 1D, classical t-state Potts model, where the Potts degrees of freedom label a spatially varying, local choice of pairing (102).[8] A disordered regime of the Potts model (with domain walls between Potts states) arises at sufficiently short times $t < t_{\mathrm{Th}}$, where $t_{\mathrm{Th}} \sim \log L$ was termed a Thouless time. For $t \gg t_{\mathrm{Th}}$, the Potts model is ordered and reproduces the ramp behavior expected from RMT.

3.3.3. Dual-unitary circuits. Dual-unitary circuits (127, 219, 228) are built up of certain classes of special two-site unitary gates that look unitary in both space-like and time-like directions. A two-qudit gate $U^{o_1 o_2}_{i_1 i_2}$ (unitarily mapping two inputs $i_{1,2}$ to two outputs $o_{1,2}$ according to arrow of time t), could alternatively be viewed sideways, according to a rotated arrow of time $\tilde{t}$, mapping input qubit states i_1, o_1 to output states i_2, o_2 as in **Figure 6*a***. The resulting map, $\tilde{U}^{i_2 o_2}_{i_1 o_1}$—called the "spacetime-dual" or "spacetime-flipped" version of U—is in general not unitary (a fact that is exploited in Section 4.2.1). However, circuits built from a special class of dual-unitary gates, for which the space–time dual is unitary (**Figure 6*b***), have come to exemplify a form of maximal chaos. Various properties such as emergence of RMT spectral correlations in the SFF (220); the dynamics of state and operator entanglement (228–233); unequal time correlation functions, both time-ordered and out-of-time-ordered (127, 197); and the eigenstate thermalization hypothesis (234, 235), etc., can be derived in such systems without any approximation and with no small parameters.

A remarkable property of these circuits is their double causal structure. Unitarity and the locality of the gates forbid correlations between points displaced by a space–time vector (x, t) if

[8] Potts symmetry is an artifact of $q \to \infty$. In general, the symmetry is that of a clock model.

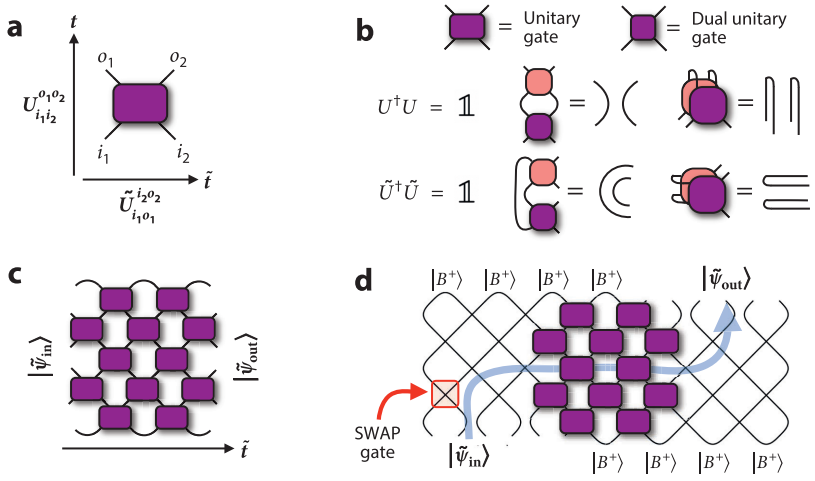

Figure 6

A generic unitary gate acting in the time direction (*a*) can be viewed as a nonunitary transformation acting in the spatial direction. A restricted class of dual-unitary gates act unitarily in both the space and time directions, as shown schematically in panel *b* (see Section 3.3.3). Generic unitary circuits give rise to a nonunitary evolution in the spatial direction (*c*), which can be thought of as unitary evolution interspersed with postselected measurement outcomes. This gives rise to a protocol outline in panel *d* for overcoming the postselection problem inherent in studying the entanglement properties of monitored pure-states, as discussed in Sections 4 and 4.2.1.

$|x| > |t|$, i.e., if the two points lie outside each other's (past or future) light cone. By the same token, however, dual unitarity rules out correlations if $|t| > |x|$, so that nonzero correlations are only possible on the ray $|x| = |t|$. This case with two arrows of time can be expanded to cases with more arrows of time (236), which may allow for more exotic analytically tractable dynamics.[9]

As discussed in Section 3.1.3, unitarity implies a simple action of the multilayer circuit on paired states. Dual unitarity implies that this also holds for the flipped evolution, and this property underlies much of the tractability of dual-unitary circuits. Writing the SFF in terms of a transfer matrix for spatial propagation, its unitarity implies the existence of t unit eigenvalues representing paired states (in this case the pairing is between a single U layer and a single U^* layer, with an arbitrary time shift in the pairing analogous to that discussed above). After averaging over an ensemble of chaotic dual-unitary circuits, these eigenvalues dominate in the limit $L \to \infty$, meaning that in these models there is no long Thouless time and the RMT result holds for finite t as $L \to \infty$ (127). The spatial transfer matrix has been investigated in more general settings in References 207, 211, 226 and 241–243.

3.3.4. Classically simulable circuits. We now consider special classes of quantum circuits that are efficiently simulable on classical computers, with simulation times scaling only polynomially, rather than exponentially, with the number of qubits. Clifford circuits, or stabilizer circuits, play an important role in quantum information theory. Clifford circuits are composed of a restricted

[9]We note that tensors with any even number of legs that are unitary under any bipartitioning of the legs (which includes dual-unitary gates as a subset) were introduced in Reference 237 as "block-perfect tensors" in the context of holographic quantum error correcting codes, in Reference 238 as "perfect tangles" for modular tensor categories, and in Reference 239 as "planar maximally entangled states." See Reference 240 for discussion of construction of dual-unitary gates.

set of quantum gates with the property that a Pauli string is mapped under Heisenberg evolution onto another Pauli string, rather than a superposition of such strings. As a result, only a single coefficient $a_S(t)$ is nonzero at each time in the expansion of the time-evolved Pauli operator in Equation 19, and the operator entanglement entropy remains zero for all times.[10] Clifford gates form a discrete subgroup of the unitary group on qudits with prime dimension $q \geq 2$. Here, we restrict our attention to Clifford circuits on qubits ($q = 2$).

The Clifford property gives an efficient way of storing a class of states (244, 245; D. Gottesman, unpublished). A stabilizer state $|\psi_S\rangle$ on L qubits is defined by L-independent and commuting Pauli string operators, the stabilizers $\{\mathcal{S}_1, \mathcal{S}_2 \cdots \mathcal{S}_L\}$, under which the state is invariant: $\mathcal{S}_i|\psi_S\rangle = |\psi_S\rangle$.[11] At any later time, $|\psi_S(t)\rangle$ is specified by the time-evolved stabilizers $\mathcal{S}_i(t) = U(t)\mathcal{S}_i U(t)^\dagger$. Each $\mathcal{S}_i(t)$ operator is a product of Pauli operators on at most L sites. Specifying the wave function through the stabilizers $\{\mathcal{S}_i(t)\}$ is efficient, requiring only $O(L^2)$ bits of information to store, even if the wave function is highly entangled; this is in contrast to the $O[\exp(L)]$ cost of storing a generic, highly-entangled state.[12] It also allows expectation values and projective measurements of Pauli string operators to be efficiently implemented and entanglement entropies to be efficiently computed (the Rényi entropies S_n are n-independent for stabilizer states).

Random unitary Clifford evolution of an initial product stabilizer state leads to ballistic growth of entanglement entropy, as in the Haar circuit. In (1+1)-dimensions this can be understood in terms of the growth of the stabilizer strings $\mathcal{S}_i(t)$ (17). The choice of stabilizers is not unique (because if $\mathcal{S}$ and $\mathcal{S}'$ are stabilizers, so is $\mathcal{S}\mathcal{S}'$), and the need to impose a convenient gauge turns the evolution of the stabilizers (and their spatial footprints) into a collective stochastic process, which has analogies to the asymmetric exclusion process for hopping particles on the line.

The time evolution operator for a Clifford circuit belongs to the Clifford group, which is a discrete subgroup of the unitary group on the full Hilbert space. This group may be generated by a small set of local Clifford gates: the two-site CNOT gate and the single-site Hadamard and Phase gates:

$$\text{CNOT} = e^{i\frac{\pi}{4}(1-Z_1)(1-X_2)}, \qquad H = (X+Z)/\sqrt{2}, \qquad P = \sqrt{Z}. \tag{26.}$$

Any multiqubit Clifford operation may be written as a product of these gates. Random Clifford circuits can be built by drawing $u_{x,\tau}$ from the set of one and two qubit Clifford gates (or from the set of generators). The Clifford gates do not form a universal gate set (i.e., there exist unitary gates that cannot be performed with Clifford operations). However, the Clifford group augmented with any gate outside of the Clifford group forms a universal gate set (40); augmenting with a single-site phase shift gate, $T = Z^{1/4}$, is sufficient, for example.

Despite their nonuniversal nature, Clifford circuits have proven to be very useful for efficiently simulating certain aspects of quantum dynamics. As an example, even though operator evolution is very special under Clifford dynamics, averaging over the ensemble of uniformly random Clifford circuits can exactly reproduce Haar averages for certain quantities such as OTOCs and right/left endpoint densities of spreading operators (50, 51). This follows from the fact that the Clifford group forms a unitary three-design (246, 247) and, hence, exactly reproduces averages involving the first three moments of the unitary group. By contrast, fluctuations of these quantities within a realization look very different between the two classes of circuits. There are other systems in which

[10]The operator entanglement entropy is computed by treating operators as states in a doubled Hilbert space, for instance, $O = \sum_{ab} O_{ab}|a\rangle\langle b| \to \sum_{ab} O_{ab}|a\rangle \otimes |b\rangle$.

[11]A simple example is a polarized state $|\uparrow, \ldots, \uparrow\rangle$, for which we can take $\mathcal{S}_i = Z_i$.

[12]The evolution of generic—nonstabilizer—states cannot be efficiently simulated even when the dynamics is Clifford.

Clifford dynamics fails to capture the essential aspects of the problem; for example, Clifford circuits with U(1) symmetry are highly restricted and only show diffusive spreading for all operators, lacking the interplay between diffusive conserved densities and ballistic operator growth discussed in Section 3.3.1.

It is worth noting that the Clifford structure relies crucially on discreteness of time. In the random circuits we started with, discrete time also allowed a key simplification, that of using the Haar measure for unitaries. However, random dynamics can also be formulated in the continuous time limit. An example is the Brownian circuit (98, 99, 140, 196, 248, 249): This is a Hamiltonian spin chain in which the couplings fluctuate like white noise. Operator spreading in continuous-time noisy models (250) is qualitatively similar to what we have discussed in Section 3.2.

The continuous time limit is also natural for noisy models of free fermions. Gaussianity is a second important structure that can be imposed on the dynamics and that leads to efficient simulability.

The quantum symmetric simple exclusion process (251–253) is a model of complex fermions hopping on the line, with noisy amplitudes, in which many quantities, for example, the moments of Green's functions in late-time nonequilibrium states, can be calculated exactly. The simplest averages map to the classical symmetric exclusion process. However, higher-order moments diagnose quantum coherences, with a nontrivial combinatorial structure. It will be interesting to study the crossover between the free fermion limit and the strongly interacting regime. (In the replica language, this is the reduction of a continuous to a discrete replica symmetry.)

Finally, automaton circuits are classically simulable circuits obtained by promoting reversible classical cellular automata to unitary quantum evolutions. In the computational basis of, say, Z eigenstates $\{|n\rangle\}$, the action of such a circuit is $U|n\rangle = e^{i\theta_n}|\pi(n)\rangle$, where $\pi \in S_{2^N}$ is a permutation of the 2^N basis states for N qubits. Although the time evolution of computational basis states is classical, these circuits can generate volume-law entanglement when acting on product states that are not computational basis states.

Automaton circuits provide a classically tractable setting in which to observe a range of interesting dynamical phenomena. First, under evolution by an automaton circuit (for, say, spin-1/2 degrees of freedom), Pauli operators can evolve into sums of products of Pauli operators, unlike in Clifford circuits. Nevertheless, the operator wave function evolves according to the same automaton circuit in a rotated basis (254). As a result, operator growth is classically tractable to study; out-of-time-ordered correlators in random, local automaton circuits, for example, (254), have been shown to exhibit growth and broadening of the operator fronts. Automaton circuits also provide a tractable setting to study subdiffusive hydrodynamics and kinetically constrained dynamics (173, 254–257), a type of measurement transition (258), and integrability (259–263). Floquet automaton circuits have also been a starting point for constructing fully quantum mechanical Floquet models with exact, nonthermal (scarred) eigenstates (264–266). A notable example is the integrable, Floquet circuit corresponding to the Rule 54 cellular automaton, which implements a simple structured dynamics involving conserved left/right moving solitons. This model captures many features of more complicated integrable systems but permits solutions of various quantities including nonequilibrium steady states, operator and entanglement spreading, and generalized hydrodynamics (259–261, 267, 268).

4. MONITORED DYNAMICS

As discussed in Section 3.1, a system of initially unentangled qubits, subjected to generic unitary gates acting on pairs of qubits, rapidly entangles, and in the long-time steady state has volume-law entanglement entropy with the maximal entropy density per qubit. At extremely long times, the

evolving pure state wave function is essentially random—sometimes called a Page state. But when such a system is monitored with repeated local measurements, this inexorable growth of entanglement is counteracted. Indeed, a single-qubit projective measurement disentangles the measured qubit. In this section, we consider the hybrid quantum circuits described in Section 2.4, in which the brickwork of unitaries is decorated with single-site measurements, placed at each space–time point with probability p. Such a structureless minimal circuit has three types of randomness: in the two-qubit unitary gates, in the locations of the projective measurements, and (more fundamentally) in the intrinsically random outcomes of the measurements, as dictated by the Born probability.

4.1. Measurement-Induced Entanglement Transition

A pure initial state, $|\psi(0)\rangle$, evolving under a hybrid circuit, defines a set of (normalized) quantum trajectories, labeled by the measurement outcomes $\mathbf{m}$:

$$|\psi_{\mathbf{m}}(t)\rangle = K_{\mathbf{m}}|\psi(0)\rangle/\sqrt{p_{\mathbf{m}}}. \qquad 27.$$

The circuit $K_{\mathbf{m}}$, consisting of unitaries interleaved with projectors, was defined in Section 2.4. The Born probability $p_{\mathbf{m}} = \langle\psi(0)|K_{\mathbf{m}}^{\dagger}K_{\mathbf{m}}|\psi(0)\rangle$ of a trajectory depends on the state, so that the monitored circuit dynamics is both nonlinear and nonunitary.

The idea of the measurement-induced transition (53, 54, 59) is that there is a qualitative change in the nature of the typical trajectories in Equation 27 as a function of the measurement rate p. When measurements are frequent, the stochastically evolving wave function is trapped by the single-spin projections, within the subspace of area-law states. (The extreme limit of this case is $p = 1$, where in each time step every qubit is measured simultaneously, giving a product state.) But when p is reduced below a threshold p_c, $|\psi\rangle$ escapes into the volume-law part of Hilbert space. At the transition itself, the evolving state has a random but scale-invariant entanglement structure. Numerical evidence for this transition has by now been found in a wide range of microscopic models (53–55, 59, 62, 63, 65–71). The efficient simulability of the Clifford circuits allows for particularly precise results there (Section 4.1.4). The transition is not specific to one dimension, and we can even consider all-to-all models without spatial locality (Sections 4.1.3 and 4.1.4).

The discrete space–time structure of the circuit lets us access a simple classical limit of the transition, which gives some intuition for how measurements inhibit the propagation of quantum correlations through space–time. We reach this classical limit by either taking $q \to \infty$ or considering the somewhat unphysical $n \to 0$ limit of the Rényi entropy S_n. In these limits, the computation of entanglement reduces to the minimal cut (Section 3.1.2), and therefore to a classical geometrical problem (53). This limit is nongeneric as far as the critical exponents (and the value of p_c) are concerned (18, 53, 67), but it captures crude features of the transition and phases.

Viewing $K_{\mathbf{m}}$ as a tensor network, a projection operator breaks a bond (it is an operator with trivial rank). For small enough p, enough bonds remain unbroken that the circuit is connected on large scales. But computing entanglement with the minimal cut, the broken bonds reduce the cut's line tension. Therefore the volume-law coefficient $s_{\text{eq}}/\ln q$ in the steady state is reduced from unity once $p > 0$. Increasing p, we eventually reach the percolation threshold in which the circuit falls apart into finite disconnected pieces. Beyond this point, the disconnected structure of the tensor network representation of $|\psi\rangle$ immediately implies that $|\psi\rangle$ cannot have long-range entanglement (a point also used in Reference 269). It also means that the line tension, setting the volume-law coefficient, has a critical vanishing at $p_c^{\text{classical}}$. At this transition, the entanglement of a subregion scales logarithmically with subregion size, a consequence of scale invariance.

Below, we discuss the properties of the phases and the critical point further; a schematic phase diagram along with the scaling of the von Neumann entanglement entropy in these phases and at

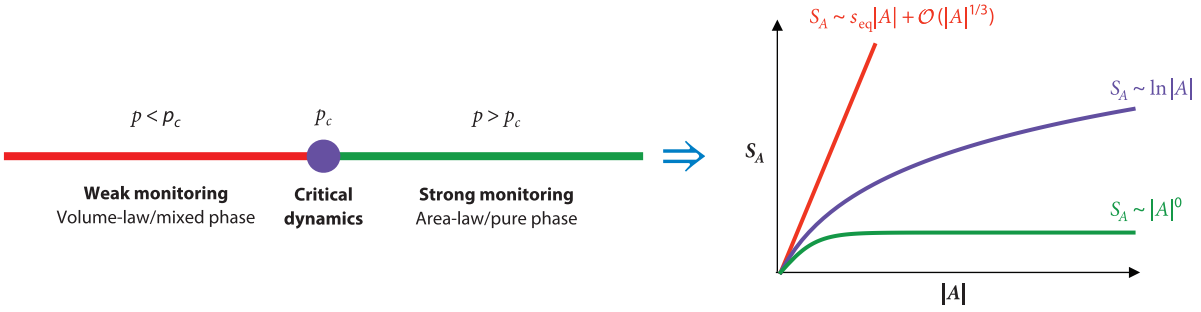

Figure 7

Monitored dynamics in (1+1)-dimensions leads to a phase transition in the entanglement properties of the pure-state trajectories as a function of the monitoring rate p, as summarized schematically on the left. The scaling of the von Neumann entanglement entropy in the steady state of the monitored dynamics with subsystem size $|A|$ in the two phases and at the entanglement phase transition is shown on the right.

the critical point in (1+1)-dimensions is summarized in **Figure 7**. The area-law phase is relatively simple: The states are product states dressed with short-range correlations. The volume-law states at $0 < p < p_c$ are nontrivial, and in particular are qualitatively different in their entanglement structure from the Page-random states that are obtained at the long time for $p = 0$ (60, 115).

Indeed, neglecting this important difference would lead to the incorrect conclusion that the volume-law phase is unstable for arbitrary small p: In a given time step, a region A suffers an extensive number of measurements ($\propto|A|$), whereas only order $|\partial A|$ unitaries act across the boundary of A and so can increase S_A. If we assumed that each measurement gave an $\mathcal{O}(1)$ decrease in S_A—which would be true for a Page state—we would conclude that measurements always win, and the volume-law state is unstable. The failure of this argument lies in the fact that the volume-law states for $0 < p < p_c$ are dissimilar to Page states, in that the change in S_A from measuring a qubit deep inside A is typically very small. This can be seen in the language of the minimal cut or more generally in terms of entanglement domain walls discussed below (Section 4.1.2).

4.1.1. Coherent trajectories versus dissipative information loss. Under the circuit dynamics, the density matrix $\rho(0)$ evolves to $\rho_{\mathbf{m}}(t) = K_{\mathbf{m}}\rho(0)K_{\mathbf{m}}^\dagger/p_{\mathbf{m}}$ with probability $p_{\mathbf{m}} = \mathrm{Tr}(K_{\mathbf{m}}^\dagger K_{\mathbf{m}}\rho(0))$. It is important to distinguish the state $\rho_{\mathbf{m}}$—which is obtained when given measurement outcomes $\mathbf{m}$ have been recorded, and which is a pure state if the initial state is pure—from the trajectory-averaged mixed state $\overline{\rho} \equiv \sum_{\mathbf{m}} p_{\mathbf{m}}\rho_{\mathbf{m}}$. (To avoid confusion, note that here the overline denotes averaging over measurements rather than over unitaries, as in previous sections.[13]) The latter density matrix would be the appropriate description of the system if there was classical uncertainty about $\mathbf{m}$—i.e., if instead of measurements (with a known outcome), we had decoherence due to interaction with an uncontrolled environment. For the dynamics we consider, $\overline{\rho}$ always tends to the trivial, infinite temperature density matrix: The rich structure of correlations in individual trajectories is washed out.

The entanglement entropy $S_A^{\mathbf{m}}$ of a subregion A, conditioned on the measurement outcomes, quantifies its correlations with the outside and is a probe of the transition, as noted above. This should be distinguished from the thermodynamic entropy of the region, defined as

[13] We imagine performing this average with the other parameters of the circuit—the choices of unitaries and measurement locations—held fixed.

$S^{\text{th}} = -\operatorname{Tr}\bar{\rho}\ln\bar{\rho}$. This tends to the maximal value even in the area-law phase, because of the additional classical uncertainty (ignorance of the measurement outcomes) implied in using $\bar{\rho}$.

Similarly, correlators of the form $\langle\mathcal{O}\mathcal{O}'\rangle_{\mathbf{m}} = \operatorname{Tr}\rho_{\mathbf{m}}\mathcal{O}\mathcal{O}'$ may be nontrivial. But trajectory-averaged correlators $\overline{\langle\mathcal{O}\mathcal{O}'\rangle_{\mathbf{m}}} = \operatorname{Tr}\bar{\rho}\mathcal{O}\mathcal{O}'$ are trivial at late times because of the triviality of $\bar{\rho}$. These statements are consistent because of cancellation between trajectories in which $\langle\mathcal{O}\mathcal{O}'\rangle_{\mathbf{m}}$ has opposite signs. This means that if we want to detect the transition using averaged correlators, we need Edwards-Anderson-like (squared) correlators, $\overline{\langle\mathcal{O}\mathcal{O}'\rangle^2_{\mathbf{m}}}$ (or other correlations involving multiple copies of a single monitored trajectory; 270.) Like the entanglement measures, these are nonlinear in the density matrix.

To measure these squared-type correlators, pairs of identical quantum trajectories (with the same measurement outcomes **m**) are required, which will generally require postselection on measurement outcomes. This is exponentially costly, requiring a number of runs exponential in the circuit's space–time volume (but see Section 4.2.1 below for an alternate type of monitored dynamics in which this postselection barrier is parametrically improved.).

Above, we viewed **m** as a record of physical measurements conducted by a hypothetical experimentalist. Quantum trajectories also arise in a quite different setting, as a formal tool for treating open quantum systems that are in contact with a decohering environment (not monitored). Assuming we do not have access to the quantum state of the environment, such a system must be described by a mixed state $\rho_{\text{open}}(t)$. In a Markovian approximation for the environment, $\rho_{\text{open}}(t)$ evolves via a quantum channel, $\rho_{\text{open}}(t) = \Phi_t[\rho_{\text{open}}(0)]$ (40). We can unravel this open system dynamics by writing $\rho_{\text{open}}(t)$ as an average over pure trajectories. In a simple case (details omitted), this leads to an ensemble formally equivalent to that discussed above. Mathematically, this is a rewriting of the channel in terms of Kraus operators $K_{\mathbf{m}}$,

$$\rho_{\text{open}}(t) = \sum_{\mathbf{m}} K_{\mathbf{m}}\rho_{\text{open}}(0)K_{\mathbf{m}}^{\dagger}, \qquad 28.$$

with $\sum_{\mathbf{m}} K_{\mathbf{m}}^{\dagger}K_{\mathbf{m}} = 1$. In this setting, the trajectories are fictitious, but they may be useful for simulating the dynamics (107–109, 271, 272). In this setting, the relevance of the measurement transition is as an easy-to-hard transition for classical simulation of various kinds of quantum processes, because the area-law states at $p > p_c$ can be efficiently represented using MPSs, whereas the highly complex volume-law states at $p < p_c$ are, a priori, exponentially costly to store and simulate. In the case with true measurements, we can think of the transition into the hard phase as an "epistemological phase transition" (58), where the wave function becomes effectively unknowable, even with access to the measurement outcomes.

4.1.2. Entanglement domain walls and the stability of the volume-law phase. In (1+1)-dimensions, the universal entanglement properties of the volume-law phase can be quantitatively described by the classical statistical mechanics of a domain wall that is equivalent to a DPRE (88). The most dramatic outcome of this correspondence is the presence of a universal subdominant contribution to the entanglement entropy in the volume-law phase, with $S_A = s_0|A| + b|A|^{\beta}$ with $\beta = 1/3$.

The simplest limit of the DPRE is the minimal cut (**Figure 2**).[14] More generally, the result can be understood using the effective 2D statistical mechanical model for replicated spins σ (defined

[14]The figure illustrates that in the presence of measurements, the minimal cut is not required to be directed on the microscopic scale. However, in the phase in which its line tension is nonzero, it is directed on large scales for energetic reasons. The same is true of the domain walls discussed below.

on the circuit's space–time manifold, with one spin for each physical gate) that label patterns of pairings between the different replicas of the circuit (55, 56). We have discussed these spins in the unitary context in Section 3.1.3, but the nonunitary nature of the monitored dynamics alters the effective statistical mechanical model. One point is that the wave function must be explicitly renormalized after each measurement when the dynamics is not unitary. More importantly, nonunitarity relaxes local constraints on the σ configurations that would follow from unitarity. In particular, the projective measurements can drive a disorder transition for σ (55, 56). We do not give a detailed exposition of the Boltzmann weights for the effective model here, but summarize some qualitative features, starting with the volume-law phase, where σ is ordered. In this phase, the model is best viewed in terms of domain walls that are forced into the 2D space–time manifold by the boundary conditions required to define the Rényi entropies (recall **Figure 3**).

Within the volume-law-entangled phase, the entanglement entropy in a subregion A can be mapped to the free energy cost, F_A, of changing the boundary conditions at the final time slice of the circuit, within the ordered phase of the statistical mechanics model. This analytic description, and the associated replica limit that is necessary to obtain the von Neumann entanglement entropy, is quantitatively similar to the replicated description of the DPRE and is thus conjectured to describe the same universal physics (88). The line tension of the resulting entanglement domain wall yields a volume-law scaling of the entanglement, $F_A = s_0|A|$, while the subdominant contribution comes from the universal fluctuations of the DPRE free energy with length, with exponent $\beta = 1/3$. This exponent, believed to be a universal feature of the volume-law phase in the presence of random unitary operators, is found numerically for the hybrid random Clifford circuit. Universal scaling functions governing the saturation of the entanglement entropy reveal the superdiffusive wandering exponent $\zeta = 2/3$ of the directed polymer. Both this exponent and the universal scaling functions extracted numerically from the DPRE are in good agreement with the numerical results obtained from the random hybrid Clifford circuit (88).

The stability of the volume-law phase against measurements is quantified by considering the reduction $\delta S(x)$ in the entanglement of a region A after performing a local measurement a distance $x \ll |A|$ away from the boundary (115). Although $\delta S(x)$ is always an $O(1)$ constant for a Page state, this quantity decays, on average, as a power law $\langle \delta S(x) \rangle \sim x^{-\Delta}$ in the volume-law phase of the monitored circuit with a consistent exponent $\Delta \approx 1.25$ observed in both the hybrid Clifford dynamics and the behavior of the corresponding observable in numerical simulations of the DPRE. With $\Delta > 1$, the total loss of entanglement after a sequence of measurements $\sim \int_0^{|A|} \delta S(x)\, dx$ is finite for large $|A|$ and can be recovered with the application of the next layer of unitaries, leading to a stable statistical steady state in the volume-law phase. We note that the average behavior of $\delta S(x)$ is dominated by rare events and that the scaling of the disorder-averaged free energy of the DPRE provides the prediction that a typical realization of the hybrid dynamics is significantly more robust, with this quantity decaying as a stretched exponential $\delta S(x) \sim \exp[-\text{const} \times x^{\beta}]$.

4.1.3. Mixed state purification transition. The transition between the volume- and area-law phases can alternatively be understood as a dynamical purification transition (56, 62, 116). For a maximally mixed initial density matrix, $\rho(0) = \mathbb{1}/2^L$, measurements at rate $p > p_c$ are able to purify the state at a system-size-independent rate (pure phase), whereas for $p < p_c$ the purification time diverges exponentially with the system size (mixed phase). These two phases correspond to the area- and volume-law phases of the circuit evolving with an initial pure state. In the mixed phase, at times polynomial in the system size there is a residual nonvanishing entropy density,

s_Q.[15] Heuristically, $s_Q L$ is the amount of quantum information propagated from the initial to the final time.

This entropy describes a dynamically evolving encoded subspace that is insensitive to future measurements—quantum information is effectively protected from single qubit measurements. For the hybrid random Clifford circuit, this corresponds to a stabilizer quantum error correcting code, denoted as (L, k, d), with L being the number of physical qubits, k being the number of encoded logical qubits, and d being the code distance—the size of the shortest logical operator. Because $k = s_Q L$ is given by the dimension of the encoded subspace, it grows linearly with L, and the code rate, $k/L \neq 0$, is finite for large L. The entanglement domain wall picture can be used to extract the code distance, which varies as L^β, coming from disorder fluctuations of the DPRE. The code rate vanishes upon approaching the pure phase—the purification transition thus corresponds to a transition in the encodability of the quantum code (57, 62, 115, 116). Although resembling a quantum error correcting code, because an efficient decoder in the presence of additional qubit errors is not known and in fact might not exist, these codes are not practical.

The purification picture also lends a natural local order parameter for the measurement transition (63). The initially maximally mixed state can be viewed as arising from tracing out a set of reference ancilla qubits that are maximally entangled with the system qubits at $t = 0$ but do not directly participate in the dynamics thereafter. The purification transition can then be probed by measuring the entanglement entropy of the reference qubits—actually one reference qubit suffices—at times $L \ll t \ll e^L$, which is nonzero in the mixed phase but vanishes in the area-law phase.

Purification is also a useful way to characterize the measurement transition for all-to-all-coupled systems of qubits, where any qubit can interact with any other (58, 62, 78). For example, the dynamics could consist of a random sequence of operations, each being (with probability p) a measurement of a random qubit or (with probability $1 - p$) a gate applied to a random pair. In this setting the volume of a subset A of spins scales the same way as its surface area (number of potential neighbors outside A), so that the volume-law coefficient $S_A/|A|$ in a pure state is not a useful diagnostic. However, the code rate s_Q above remains a valid order parameter for the transition.

4.1.4. The critical point. The entanglement transition between the area- and volume-law phases is a continuous phase transition and can be explored both numerically and, in some instances, analytically. Detailed large-scale numerical simulations are possible on hybrid random Clifford circuits (with two-site unitaries drawn randomly from the Clifford group and single-site Pauli measurements) and reveal the existence of a finite critical measurement rate, $p_c \approx 0.17$ in 1+1-dimensions (113), separating a volume-law entangled phase for $p < p_c$ from an area-law phase when $p > p_c$, as shown in **Figure 7**. The critical point has a dynamical exponent $z = 1$ and in 1+1-dimensions exhibits a conformal symmetry (68, 71). Simulations with Haar random gates or in general Hamiltonian models are restricted to much smaller sizes but are also consistent with a continuous transition with $z = 1$ (67, 68).

When the qubits are extended to qudits, with dimension $q \to \infty$, analytic progress is possible, because as discussed above the phase transition in this limit maps to the problem of a minimal cut through a percolation configuration (18, 53). The critical exponents are then those of the nonunitary conformal field theory for percolation. However, the percolation fixed point is unstable

[15] In the minimal cut/domain wall picture, this is related to the cost of a horizontal domain wall that separates the initial from the final time (56–58) and which measures the "entanglement" between the initial and final time boundaries of the nonunitary circuit. This shows that s_Q is also equal to the pure state volume-law coefficient.

for finite q, and the critical properties are in general analytically intractable, though expected still to be conformal.

It is natural to ask for a Landau–Ginsburg-like field theory for the measurement transition. This is closely connected to the problem of formulating a field theory for the entanglement transition in an RTN (141; an RTN, with virtual bonds in the bulk and physical bonds on the boundary, can undergo an entanglement phase transition as a function of the distribution of local tensors) though there is a key difference related to Born's rule.

At first sight, we might think that a field theory could be inferred immediately from the effective lattice magnet, mentioned above, for the degree of freedom $\sigma \in S_N$. This formalism is powerful in the ordered/entangling phase, where we can work with domain walls, and gives a useful magnetic analogy for the critical point, but it is more challenging to coarse-grain σ to arrive at a continuum theory near the critical point. This is because of the need for the replica trick[16] (55, 56, 58, 141): Disorder averages must be handled by analytically continuing the lattice magnet to unphysical values of N, where the target space S_N for σ collapses to nothing[17] (see Reference 18 for a review).

Effective lattice models can be formulated for both the measurement-induced phase transition (MIPT) and the RTN (55, 56, 141). Each case has the G_N layer-permutation symmetry that we met in Section 3.1.3, but the required replica limits are $N \to 1$ for the MIPT and $N \to 0$ for the RTN. This difference arises from the fact that averages for the MIPT, unlike the RTN, must include the Born probability $\langle\psi| K_{\mathbf{m}}^\dagger K_{\mathbf{m}} |\psi\rangle$. This factor involves one layer each of the circuit $K_{\mathbf{m}}$ and its conjugate $K_{\mathbf{m}}^*$ (see Section 3.1.3), so it increases N by 1.

It is possible to view the models of interest, with G_N symmetry, as symmetry-breaking perturbations of a Potts model with $Q = N!$ states (141). This means initially treating all the $N!$ possible values for σ as equivalent, giving a larger $S_{N!}$ symmetry.[18] The Landau–Ginsburg theory for Potts is well understood (274). However, reducing the symmetry to the physical symmetry, $G_N \subset S_{N!}$, introduces an infinite number of relevant perturbations that are not related to each other by G_N symmetry. This means that it is not easy to control the RG flow away from the Potts fixed point.

The basic issue is that σ splits into an infinite number of distinct representations[19] of G_N, and one must decide which should be retained as fundamental fields in a Lagrangian (58). An alternative approach is motivated by the picture of overlaps between Feynman trajectories discussed in previous sections. We can introduce an Edwards-Anderson-like matrix order parameter, X_{ab}, which characterizes the strength of overlap between forward layer a and backward layer b (58). (Different values of σ correspond to different ordered states for X.) X transforms simply under G_N, and using this one can write putative Landau–Ginsburg Lagrangians $\mathcal{L}(X)$ for the MIPT and RTN. It remains to be seen whether these conjectured theories describe the physical problems of interest.

---

[16] In Section 3.1.3, we sketched a mapping of S_2 to a domain wall free energy that avoided the replica trick. This used the fact that clusters of "$\perp$" spins were of finite typical size, rather than proliferating in space–time. This approach continues to hold in the entangled phase in the presence of measurements (58), but not at the critical point, where the typical size of $\perp$ clusters diverges.

[17] For heuristic motivation, recall a simpler use of the replica trick for averages in disordered systems. Let Z be a partition function for a classical field, ϕ, with random couplings. The averaged free energy may be written as $\overline{\ln Z} = \lim_{N\to 0}(\overline{Z^N} - 1)/N$. On the right-hand side, $\overline{Z^N}$ is a partition function for N copies of the field, which we can arrange as a vector $\phi = (\phi_1, \ldots, \phi_N)$. The right-hand side requires us to take the limit of the vanishing number of components.

[18] In the limits $N \to 0$ and $N \to 1$, this becomes a $Q = 1$ state Potts model (141), which is a representation of percolation (273). However—confusingly—this percolation fixed point is distinct from the minimal cut limit discussed above (it does not correspond to a physical limit of the original problem).

[19] Here, we regard σ as an element of the group algebra; i.e., we allow ourselves to take linear combinations as is natural if we want to coarse-grain.

Given these complications, it is natural to look for ways to simplify the transition. One is to get rid of spatial locality (58, 62, 78). As noted above, there is no meaning to volume law versus area law in all-to-all models, but purification (the amount of information propagated between initial and final times) can be used to distinguish the phases.

In the limit $q \to \infty$, the all-to-all model mentioned at the end of Section 4.1.3 maps to a minimal cut problem in a classical graph with temporal, but not spatial, locality. This is solvable essentially by percolation mean-field theory (58, 62). A model with "instantaneous quantum polynomial time" (275, p. 1415) gates (276) shows another transition, described by mean-field percolation on a time slice (78).

At finite q, we can try to exploit the space–time geometry of the all-to-all quantum circuit. This is locally tree-like: The only loops have a size that diverges in the thermodynamic limit (as in many random graph ensembles; 277). This suggests that the MIPT coincides with the entanglement transition of an ensemble of tree tensor networks (58, 87) with the same local structure. If, as a simplification, the measurement outcomes in the parent circuit are fixed using postselection (instead of sampled with Born's rule), this tree transition is exactly solvable (58; as are a broader class of entanglement transitions for tree tensor networks). The natural entanglement order parameter vanishes in a strongly nonmean-field fashion as $\exp(-c/\sqrt{p - p_c})$. These all-to-all models are perhaps the simplest incarnations of the MIPT and deserve further study.

4.2. Structured Monitored Circuits

There is a rich landscape of monitored dynamics beyond the minimally structured case of random two-qubit unitary gates interspersed with single-site measurements. A simple extension is to consider dynamics with only multisite measurements and no unitary gates. Monitored pure states in measurement-only dynamics can also display phase transitions between volume- and area-law scaling of the entanglement entropy (72). This is striking because there are no unitary gates in these models to compete with the measurements; rather, the scrambling and unscrambling are inextricably intertwined, and the principle driving the transition is the mutual incompatibility or frustration of the measurement operators.

A further extension of unstructured, monitored dynamics is to consider symmetry-enriched monitored dynamics, obtained by restricting the unitary gates and measurements to operations that respect an on-site global symmetry G (72–74, 278). Such models can still display an entanglement phase transition from area- to volume-law entangled steady state ensembles; however, the symmetry structure of the replicated statistical mechanical description is enlarged by combining the circuit symmetry G with the intrinsic dynamical symmetries of the problem (cf. Equation 18). This permits novel types of dynamical orders that transcend the phase classifications obtained in the more conventional setting of static (or even Floquet) Hamiltonians with the same symmetry G. One upshot is that we can obtain multiple varieties of both area- and volume-law phases—for instance, distinguished by the presence or absence of different types of long-range symmetry-breaking orders or symmetry-protected topological orders—with phase transitions between these occurring within the area- and volume-law entangled phases. Importantly, these orders are only observable in nonlinear Edwards-Anderson-type order parameters that measure fluctuations across trajectories, whereas simple averages remain featureless.

It is illustrative to discuss an example of a phase transition between area-law states in a system with Ising symmetry $G = \mathbb{Z}_2$ (74); related to the measurement-only Majorana model in Reference 64. This example is reminiscent of a ground-state phase transition from a paramagnet to a symmetry-broken ferromagnet, although a closer analogy may be the eigenstate phase transition between spin-glass ordered and paramagnetic states in many-body localized systems

(279, 280). We consider measurement-only Clifford dynamics in a 1D spin-1/2 system. There are no unitary gates, and measurements are drawn randomly in space–time from two sets of commuting operators: with probability p_Z from $\{Z_iZ_{i+1}\}$ and with probability $p_X = 1 - p_Z$ from $\{X_i\}$. Each operator in the ensemble commutes with the symmetry generator $P = \Pi_i X_i$, and we start with a symmetric initial state such as a product state in the X basis. When $p_Z = 1$, the dynamics measures Z_iZ_{i+1} on each bond, which projects onto Schrödinger cat states with long-range spin-glass order and area-law entanglement. A particular trajectory leads to a random sequence of measurement outcomes, $m_i = \pm 1$, on each bond; there are two symmetry-broken product states in the Z basis consistent with these outcomes (and related by the action of P), and the output state is a symmetric/antisymmetric cat superposition of these states, depending on the symmetry of the initial state. For example, if $m_i = \{+1, -1, +1\}$ in a system of length $L = 4$, the output state is $|\psi_{\mathbf{m}}\rangle \propto |\uparrow\uparrow\downarrow\downarrow\rangle \pm |\downarrow\downarrow\uparrow\uparrow\rangle$. The order refers to the random orientation of spins (which generalizes the aligned pattern of a conventional ferromagnet); the long-range order is diagnosed by an Edwards–Anderson order parameter, $\chi^{\mathrm{SG}} = \lim_{L\to\infty} \sum_{\mathbf{m}} p_{\mathbf{m}} \frac{1}{L^2} \sum_{ij} \langle \psi_{\mathbf{m}} | Z_i Z_j | \psi_{\mathbf{m}} \rangle^2 > 0$. In contrast, when $p_X = 1$, we measure X_i on every site, and the output state is a paramagnetic product state in the X basis with $\chi^{\mathrm{SG}} \to 0$. There is no volume-law phase in this model, and a dynamical phase transition between the paramagnetic and ordered area-law states occurs at $p_Z = 0.5$.

When the discrete Ising symmetry is replaced by a continuous symmetry, such as a global U(1) symmetry, the phase structure appears to be even richer (281). For a U(1) circuit with symmetry respecting two-qubit unitary gates and single-site Z_i measurements, the volume-law phase has been predicted to break into two phases, a "charge-fuzzy" phase and a "charge-sharp" phase. In the former, which occurs at small measurement rate p, an initial pure state that is a linear combination of different charge sectors (for example, all spins pointing in the X direction) evolves into a charge eigenstate on times that are linear in the number of qubits. By contrast, in the the charge-sharp phase at higher p (but still in the volume-law phase), this charge sharpening occurs on times that are of order one for large system size. One can also consider an ancilla coupled to two different charge sectors, namely $|\Psi\rangle = |\psi_Q\rangle|0\rangle + |\psi_{Q-1}\rangle|1\rangle$, with $|\psi_Q\rangle$ representing a state in the charge Q sector (while $|0\rangle$ and $|1\rangle$ are states of the ancilla). In this case, the ancilla qubit purifies on timescales of order one in the charge-sharp phase, but more slowly, of order L in the charge-fuzzy phase. A proposed field theory predicts an infinite-order (Kosterlitz–Thouless) phase transition between the charge-sharp and charge-fuzzy phases (282). Further explorations of circuits with U(1) symmetry, or other non-Abelian symmetries, constitutes an exciting future direction.

Monitored dynamics can drive phase transitions between states with distinct topological quantum orders (72, 75–77). As an example, measurements of the stabilizers of the toric code (283), along with a weak rate of single-qubit measurements in the Pauli basis, can give rise to an area-law entangled, topologically ordered phase in which the monitored pure states sustain long-range entanglement that cannot be removed by a finite-depth unitary circuit, as quantified by a topological entanglement entropy (284, 285) of $S_{\mathrm{topo}} = 2 \ln 2$. Equivalently, in the purifying dynamics of a maximally mixed initial state, the entanglement entropy of the system saturates to $S = S_{\mathrm{topo}}$ in constant time, and the system fails to completely purify up to times that scale exponentially in the linear dimension of the system.

Monitored dynamics is also interesting for dynamics with free fermion structure (58, 60, 61, 64, 66, 82, 91, 286–288), in which unitary evolution and measurements of fermion bilinears only lead to the generation of two-body correlations. In contrast to a generic monitored dynamics, free fermion–monitored evolution cannot sustain a volume-law-entangled phase for any nonzero monitoring rate in any number of spatial dimensions (61). This is related to having a continuous rather than discrete replica symmetry, which reduces the cost of entanglement domain walls (58). Equivalently, it has been shown that the purification time for an N-fermion state is at most

$O(N^2)$, so that free-fermion monitored systems purify much faster than interaciting systems at weak monitoring (58, 287).

Apart from area-law entangled steady states, however, both the continuous- and discrete-time monitored dynamics of free fermions can give rise to superarea-law (logarithmic in 1D) entangled phases and critical points separating these from area-law phases (64, 66, 82).

4.2.1. Hybrid dynamics from space–time duality. We now consider a special class of monitored dynamics obtained via a space–time rotation of unitary dynamics (79–81). These afford various benefits, both in the postselection cost of selecting quantum trajectories and in furnishing a complementary analytic perspective relating monitored and unitary dynamics.

As discussed in Section 3.3.3, viewing a unitary quantum gate $U^{o_1 o_2}_{i_1 i_2}$ sideways generically results in a nonunitary map, $\tilde{U}^{i_2 o_2}_{i_1 o_1}$. This map implements a forced or postselected measurement: A specific unitary gate yields a specific fixed measurement outcome with no Born randomness. For example, if U is a two-site identity gate, its dual $\tilde{\mathbb{1}} = 2\left|B^+\right\rangle\left\langle B^+\right|$ is proportional to a projection onto a specific Bell pair state $\left|B^+\right\rangle \equiv \frac{1}{\sqrt{2}}(|\uparrow\uparrow\rangle + |\downarrow\downarrow\rangle)$.[20] Performing this exchange in the roles of space and time across the entire circuit associates to every unitary evolution a nonunitary partner. The input and output states of the dual monitored evolution live on time-like slices and correspond to spatial boundary conditions of the unitary evolution, as shown in **Figure 6*c***.

Thus far, this seems to be a purely theoretical construction—after all, an experimentalist cannot directly implement forced measurements like $\tilde{\mathbb{1}}$ (except by costly postselection). However, a simple protocol described in Reference 80 uses a teleportation protocol to transfer the time-like input/output states to conventional space-like slices at the cost of introducing additional ancilla qubits and unitary SWAP gates; the system and ancilla qubits are then evolved with purely unitary gates (which the experimentalist *does* have access to); following this evolution, a set of postselected Bell measurements at the final time slice produces the desired output state corresponding to sideways hybrid evolution as shown in **Figure 6*d***. Thus, though these circuits do not eliminate the postselection problem, they parametrically improve the cost by only requiring postselection at the final time rather than the entire space–time volume; this is also desirable for various near-term experimental architectures that do not allow measurements in the middle of the circuit but only at the end.

Separately, flipped circuits provide a useful analytic perspective on monitored circuits by bootstrapping to the vast body of knowledge on temporal entanglement dynamics in unitary circuits. To zeroth order, space–time duality exchanges the roles of space and time; hence, spatial scaling of entanglement in the late-time states of flipped monitored circuits maps to the temporal scaling of entanglement growth in the corresponding unitary circuit (80, 81). If the unitary circuit is chaotic and displays ballistic entanglement growth $S(t) \sim v_E t$, this translates to a volume-law scaling for steady states in the flipped circuits, with an entropy density set by v_E, $\tilde{S}_A(\tilde{t} \to \infty) \sim v_E|A|$. Interestingly, this also implies that the variety of temporal entanglement dynamics in unitary settings (ranging from logarithmic to subballistic growth in time) translate to different spatial scalings in the output states (ranging from logarithmic to fractal), leading to new classes of entanglement phases in monitored dynamics.

Importantly, however, the interchanging of space and time is not the full story. The scaling of subsystem entanglement in output states of monitored dynamics is mapped to the temporal

[20] In general, a polar decomposition yields $\tilde{U} = 2FW$, where W is a unitary gate, and F is positive semidefinite and normalized to $\mathrm{Tr}(F^2) = 1$. Because $F \geq 0$, we can interpret $\tilde{U}$ as an element of a positive operator-valued measure (POVM): It corresponds to a forced weak measurement (i.e., deterministically postselecting a particular outcome of a POVM).

growth of entanglement in unitary circuits, but the unitary evolution is accompanied by boundary decoherence, which allows information to escape the system and be radiated away from one of its edges (80). This furnishes a connection between monitored and dissipative dynamics, which were contrasted in Section 4.1.1. The presence of boundary dissipation furnishes universal subleading corrections to the leading entanglement scaling that, for instance, characterize the nonthermal nature of the volume-law phase. For example, the entropy of a mixed state evolving under Haar random unitaries subject to boundary dissipation can be calculated using the domain wall picture described in Section 3.1.3, with the domain wall pinned to the boundary of the system at the final time. The edge dissipation changes the random walk calculation discussed earlier by introducing a partially absorbing boundary condition. This analysis furnishes subleading corrections to the temporal entanglement dynamics, coming from both the $t^{1/3}$ KPZ corrections present in the quenched average of entanglement and an additional $3/2\log(t)$ piece from the partially absorbing boundary conditions. Upon dualizing, these give the same $|A|^{1/3}$ spatial corrections to the entanglement entropy of the volume-law states obtained via the DPRE picture in Section 4.1.2; indeed, in this setting, one could think of the domain wall picture as a microscopic realization of the (DPRE) effective description.

5. EXPERIMENTS

The subject of this review is topical in light of rapid experimental progress in building programmable digital quantum simulators. The ability to isolate quantum-coherent qubits; to couple qubits via controlled unitary operations; and to make high-fidelity locally resolved measurements for readout, control, and feedback all represent major engineering challenges. These challenges are being actively pursued over several physical platforms ranging from superconducting junctions to trapped ions. Although much of this effort is broadly motivated by the quest to build universal programmable quantum computers—a goal that is still far in the future given current parameters for noise rates and system sizes (39)—these platforms have already furnished impressive new capabilities when viewed as experimental platforms for many-body physics. This dual view of a computational device as an information-theoretic tool, on one hand, and a real experimental system for many-body physics, on the other, is reflected in the broad interdisciplinary theoretical interest in quantum circuits.

One of the first experimental breakthroughs in digital simulation was Google's announcement of "quantum supremacy" in a 53-qubit system (132, p. 505), signaling a leap from a decades-long effort in designing and benchmarking individual quantum circuit elements to the arrival of genuinely many-body coupled systems with vast Hilbert spaces. An abstract information-theoretic task was chosen for the demonstration, that of sampling from the output distribution of a state evolved under a random quantum circuit (131, 289–291); the task illustrates the utility of quantum circuit dynamics for benchmarking near-term quantum devices.

From the point of view of many-body physics, it is particularly interesting to study phenomena in the regimes opened up by the natural operational mode of these devices that is accessible in the present-term, i.e., viewing them as quantum circuits executing nonequilibrium dynamics (292; as opposed to universal simulators that may eventually shed light on long-standing equilibrium problems in strongly correlated physics, such as the phase diagram of the 2D Hubbard model). These platforms are also building remarkable capabilities to access the new types of information-theoretic observables we have discussed in this review. Tomographic techniques, though strongly limited to small system sizes, allow the full reconstruction of a density matrix—including quantum-coherent off-diagonal terms—and thereby allow the computation of any nonlinear function of the density matrix, including entanglement. A beautiful experiment on an (analog) Bose–Hubbard

simulator (293, 294) computed the purity, $\langle \mathrm{Tr}\rho_A^2 \rangle = \mathrm{Tr}(\mathrm{SWAP}_A \rho \otimes \rho)$, by making two identical copies of a system and measuring a partial SWAP operator between the two copies (295, 296), circumventing the need for tomography at the expense of needing to prepare multiple copies. Novel ancilla-assisted measurement protocols (like the Hadamard test) can implement new types of correlation functions.

These capabilities have been put to use in several notable recent works. We focus here on experiments with quantum circuits, but note that these works follow many milestone papers probing fundamental aspects of quantum dynamics, thermalization, and MBL on a wide variety of analog simulator platforms (36, 294, 297–302). Reference 303 furnished a detailed experimental study of information scrambling in a variety of chaotic quantum circuits by measuring out-of-time-ordered commutators using ancilla-assisted methods. Reference 304 implemented a circuit to prepare the ground state of the topologically ordered toric code, performed a measurement of the topological entanglement entropy of the state, and simulated an anyon braiding operation on the state. Reference 305 implemented an MBL Floquet circuit to simulate a time crystal and made an ancilla-assisted measurement of a spectrum-averaged unequal space–time correlation function closely related to the Edwards–Anderson correlator discussed previously; this correlator probes the defining spatiotemporal order of the phase across the entire exponentially dense many-body spectrum and contrasts with conventional correlators that vanish on taking an infinite temperature average over the entire spectrum.

When considering monitored circuits with unitaries and measurements, we must reckon with the prohibitive postselection barrier mentioned earlier. Here, the challenge of preparing multiple copies of a given quantum state (i.e., a given trajectory associated with a specific set of measurement outcomes $\mathbf{m}$) is not merely an engineering one but a fundamental theoretical one stemming from the randomness inherent to the measurement process. Reference 306 made a first experimental attempt to probe this physics in a small 8-qubit trapped ion system by measuring the late-time entanglement entropy of a reference qubit entangled with the system at $t = 0$, as discussed in Section 4.1.3. This method requires the existence of a decoder to correlate the basis in which the reference qubit is measured with the measurement record on the system, which was achieved in the experiment by using Clifford circuits whose classical simulability allows wrong measurement outcomes to be corrected by a feed-forward action determining future unitary operations. On small enough systems, individual trajectories can be reproduced by brute-force, as was done in a recent experiment using IBM's digital simulators (307). However, larger-scale experimental demonstrations of non-Clifford monitored evolutions will require fundamental new approaches to address the postselection problem, for instance, by appealing to additional structures like space–time duality that can parametrically reduce postselection overhead as discussed in Section 4.2.1.

6. OUTLOOK

We conclude by outlining some important topic areas and questions within quantum circuit dynamics that deserve further study. First, the effects of feedback in quantum dynamics—whereby future unitary operations or measurements are conditioned on past measurement outcomes—remain to be understood. How can feedback be harnessed to stabilize ordered phases of quantum matter in quantum circuit dynamics, and how can these protocols be realized in digital quantum simulators? How does feedback affect the generation of quantum many-body entanglement? Quantum error-correction (40) provides one well-studied example of the powerful effects of feedback, which can allow an observer to recover an unknown quantum state encoded in an evolving quantum system, though a more extensive exploration of this new area of interactive quantum

dynamics is warranted.[21] The out-of-equilibrium phases that can arise owing to the interplay of monitored dynamics with open quantum system dynamics, which evolve the system of interest into a mixed state, are beginning to be explored (83, 88, 308, 309) and also provide a fruitful area of study.

In the study of monitored quantum circuits, probing the entanglement properties of monitored pure states generally requires a large amount of postselection, as explained in Section 4.1.1, which presents a barrier for observing the measurement-driven entanglement phase transition experimentally. Are there classes of monitored dynamics, apart from Clifford dynamics and evolution with a dual-unitary description (79), in which this postselection barrier can be avoided? Can space–time rotations of unitary quantum circuits (80, 81) be used to overcome postselection problems in the preparation of other interesting kinds of quantum states?

The entanglement phase transition in monitored dynamics remains to be fully characterized. In the Clifford case, a quantitative understanding of the evolution of stabilizers (Section 3.3.4) in monitored Clifford circuits might shed light on this transition. Progress in understanding the relevant statistical mechanical descriptions of monitored systems with continuous symmetries would also provide useful insight into phases that can arise in this setting. As we touched on in Section 4, there are also interesting questions about coarse-graining the effective models for the case of generic unitaries, with connections to fundamental concepts in the theory of disordered systems. Separately, it would be interesting to have mathematically rigorous results for the phase diagram of the measurement problem, for example, a rigorous proof of the stability of the volume-law phase.

At the level of formalism there is also much still to understand about the structure of the effective lattice models for both unitary and nonunitary dynamics, for example, about the combinatorial structure underlying various replica-like limits. Although we have discussed here a limited number of quantities, this formalism can be applied to almost any observable of interest in the circuit.

As we discussed at the outset, one way to motivate the circuits is as simpler models for dynamics in more conventional many-body systems with a fixed Hamiltonian, either on the lattice or in the continuum. In Sections 3.1.3 and 3.3.2, we touched on some ways of extending ideas from the random circuit to nonrandom systems, but there is much still to do here.

Finally, can monitored dynamics provide (*a*) new benchmarking tasks for near-term quantum computers or (*b*) insights into quantum error-correcting codes? Time-periodic monitored dynamics have been recently used to construct dynamically evolving, fault-tolerant quantum codes (310, 311), though it remains to be understood if other kinds of monitored evolution can produce similarly useful codes in which decoding quantum information is practical and feasible.

DISCLOSURE STATEMENT

The authors are not aware of any affiliations, memberships, funding, or financial holdings that might be perceived as affecting the objectivity of this review.

ACKNOWLEDGMENTS

We thank Ehud Altman, Denis Bernard, Bruno Bertini, John Chalker, Amos Chan, Xiao Chen, Andrea De Luca, Fabian Essler, Ruihua Fan, Zongping Gong, Sarang Gopalakrishnan, Michael Gullans, Jeongwan Haah, Timothy Hsieh, David Huse, Matteo Ippoliti, Cheryne Jonay,

[21] We note that successful quantum error correction would lead to the recovery of a particular encoded quantum state with high fidelity, which is a priori a much more stringent requirement than using feedback to stabilize a phase of a quantum many-body system.

Yaodong Li, Andrew Lucas, Andreas Ludwig, Roderich Moessner, Rahul Nandkishore, Lorenzo Piroli, Tomaz Prosen, Tibor Rakovszky, Sthitadhi Roy, Jonathan Ruhman, Shengqi Sang, Brian Skinner, Shivaji Sondhi, Tobias Swann, Romain Vasseur, Ashvin Vishwanath, Curt von Keyserlingk, Zhi-Cheng Yang, Yi-Zhuang You, Tianci Zhou, and Marko Znidaric for collaboration on related work and/or fruitful discussions.

V.K. acknowledges support from the Sloan Foundation through a Sloan Research Fellowship and the Packard Foundation through a Packard Fellowship and by the US Department of Energy, Office of Science, Basic Energy Sciences, under Early Career Award No. DE-SC0021111. V.K. thanks the Kavli Institute of Theoretical Physics (KITP) for hospitality during a part of this project. KITP is supported in part by the National Science Foundation under Grant No. NSF PHY-1748958. M.P.A.F. gratefully acknowledges support from the Heising–Simons Foundation and by the Simons Collaboration on Ultra-Quantum Matter, which is a grant from the Simons Foundation (651440).

LITERATURE CITED

1. D'Alessio L, Kafri Y, Polkovnikov A, Rigol M. 2016. *Adv. Phys.* 65(3):239–362
2. Nandkishore R, Huse DA. 2015. *Annu. Rev. Condens. Matter Phys.* 6:15–38
3. Abanin DA, Altman E, Bloch I, Serbyn M. 2019. *Rev. Mod. Phys.* 91(2):021001
4. Serbyn M, Abanin DA, Papić Z. 2021. *Nat. Phys.* 17(6):675–85
5. Moudgalya S, Bernevig BA, Regnault N. 2022. *Rep. Prog. Phys.* 85:086501
6. Chandran A, Iadecola T, Khemani V, Moessner R. 2023. *Annu. Rev. Condens. Matter Phys.* 14:443–69
7. Doyon B. 2020. *SciPost Phys. Lect. Notes* 2020:18
8. Bulchandani VB, Gopalakrishnan S, Ilievski E. 2021. *J. Stat. Mech. Theory Exp.* 2021(8):084001
9. Fagotti M, Calabrese P. 2008. *Phys. Rev. A* 78:010306
10. Buyskikh AS, Fagotti M, Schachenmayer J, Essler F, Daley AJ. 2016. *Phys. Rev. A* 93(5):053620
11. Läuchli AM, Kollath C. 2008. *J. Stat. Mech. Theory Exp.* 2008(05):P05018
12. Kim H, Huse DA. 2013. *Phys. Rev. Lett.* 111(12):127205
13. Ho WW, Abanin DA. 2017. *Phys. Rev. B* 95(9):094302
14. Bardarson JH, Pollmann F, Moore JE. 2012. *Phys. Rev. Lett.* 109:017202
15. Serbyn M, Papić Z, Abanin DA. 2013. *Phys. Rev. Lett.* 110(26):260601
16. Huse DA, Nandkishore R, Oganesyan V. 2014. *Phys. Rev. B* 90(17):174202
17. Nahum A, Ruhman J, Vijay S, Haah J. 2017. *Phys. Rev. X* 7(3):031016
18. Potter AC, Vasseur R. 2022. In *Entanglement in Spin Chains. Quantum Science and Technology*, ed. A Bayat, S Bose, H Johannesson, pp. 211–49. Cham, Switz.: Springer
19. Calabrese P, Cardy J. 2005. *J. Stat. Mech. Theory Exp.* 2005(04):P04010
20. Calabrese P, Cardy J. 2009. *J. Phys. Math. Theor.* 42(50):504005
21. Asplund CT, Bernamonti A, Galli F, Hartman T. 2015. *J. High Energy Phys.* 2015(9):110
22. Liu H, Suh SJ. 2014. *Phys. Rev. Lett.* 112:011601
23. Hayden P, Preskill J. 2007. *J. High Energy Phys.* 2007(9):120
24. Roberts DA, Stanford D, Susskind L. 2015. *J. High Energy Phys.* 2015(3):51
25. Abajo-Arrastia J, Aparicio J, López E. 2010. *J. High Energy Phys.* 2010(11):149
26. Hartman T, Maldacena J. 2013. *J. High Energy Phys.* 2013(5):14
27. Hubeny VE, Rangamani M, Takayanagi T. 2007. *J. High Energy Phys.* 2007(7):062
28. Altman E, Brown KR, Carleo G, Carr LD, Demler E, et al. 2021. *PRX Quantum* 2:017003
29. Lewenstein M, Sanpera A, Ahufinger V, Damski B, Sen A, Sen U. 2007. *Adv. Phys.* 56(2):243–379
30. Schäfer F, Fukuhara T, Sugawa S, Takasu Y, Takahashi Y. 2020. *Nat. Rev. Phys.* 2(8):411–25
31. Gross C, Bloch I. 2017. *Science* 357(6355):995–1001
32. Browaeys A, Lahaye T. 2020. *Nat. Phys.* 16(2):132–42
33. Blatt R, Roos CF. 2012. *Nat. Phys.* 8(4):277–84
34. Lanyon BP, Hempel C, Nigg D, Müller M, Gerritsma R, et al. 2011. *Science* 334(6052):57–61

35. Gogolin C, Eisert J. 2016. *Rep. Prog. Phys.* 79(5):056001
36. Schreiber M, Hodgman SS, Bordia P, Lüschen HP, Fischer MH, et al. 2015. *Science* 349(6250):842–45
37. Wendin G. 2017. *Rep. Prog. Phys.* 80(10):106001
38. Kjaergaard M, Schwartz ME, Braumüller J, Krantz P, Wang JIJ, et al. 2020. *Annu. Rev. Condens. Matter Phys.* 11:369–95
39. Preskill J. 2018. *Quantum* 2:79
40. Nielson MA, Chuang IL. 2000. *Quantum Computation and Quantum Information*. Cambridge, UK: Cambridge Univ. Press
41. Deutsch JM. 1991. *Phys. Rev. A* 43(4):2046–49
42. Srednicki M. 1994. *Phys. Rev. E* 50(2):888–901
43. Rigol M, Dunjko V, Olshanii M. 2008. *Nature* 452(7189):854–58
44. Wen XG. 2017. *Rev. Mod. Phys.* 89(4):041004
45. Eisert J, Cramer M, Plenio MB. 2010. *Rev. Mod. Phys.* 82:277
46. Swingle B. 2010. *Phys. Rev. Lett.* 105(5):050502
47. Harrow AW, Montanaro A. 2017. *Nature* 549(7671):203–9
48. Brody TA, Flores J, French JB, Mello P, Pandey A, Wong SS. 1981. *Rev. Mod. Phys.* 53(3):385–479
49. Beenakker CW. 1997. *Rev. Mod. Phys.* 69(3):731–808
50. Nahum A, Vijay S, Haah J. 2018. *Phys. Rev. X* 8(2):021014
51. Von Keyserlingk C, Rakovszky T, Pollmann F, Sondhi SL. 2018. *Phys. Rev. X* 8(2):021013
52. Zhou T, Nahum A. 2020. *Phys. Rev. X* 10(3):031066
53. Skinner B, Ruhman J, Nahum A. 2019. *Phys. Rev. X* 9(3):031009
54. Li Y, Chen X, Fisher MPA. 2018. *Phys. Rev. B* 98(20):205136
55. Jian CM, You YZ, Vasseur R, Ludwig AW. 2020. *Phys. Rev. B* 101(10):104302
56. Bao Y, Choi S, Altman E. 2020. *Phys. Rev. B* 101(10):104301
57. Li Y, Fisher MPA. 2021. *Phys. Rev. B* 103(10):104306
58. Nahum A, Roy S, Skinner B, Ruhman J. 2021. *PRX Quantum* 2:010352
59. Li Y, Chen X, Fisher MPA. 2019. *Phys. Rev. B* 100(13):134306
60. Chan A, Nandkishore RM, Pretko M, Smith G. 2019. *Phys. Rev. B* 99(22):224307
61. Cao X, Tilloy A, De Luca A. 2019. *SciPost Phys.* 7:024
62. Gullans MJ, Huse DA. 2020. *Phys. Rev. X* 10(4):041020
63. Gullans MJ, Huse DA. 2020. *Phys. Rev. Lett.* 125(7):070606
64. Nahum A, Skinner B. 2020. *Phys. Rev. Res.* 2(2):023288
65. Szyniszewski M, Romito A, Schomerus H. 2019. *Phys. Rev. B* 100(6):064204
66. Chen X, Li Y, Fisher MPA, Lucas A. 2020. *Phys. Rev. Res.* 2(3):033017
67. Zabalo A, Gullans MJ, Wilson JH, Gopalakrishnan S, Huse DA, Pixley J. 2020. *Phys. Rev. B* 101(6):060301
68. Zabalo A, Gullans MJ, Wilson JH, Vasseur R, Ludwig AW, et al. 2022. *Phys. Rev. Lett.* 128(5):050602
69. Turkeshi X, Fazio R, Dalmonte M. 2020. *Phys. Rev. B* 102:014315
70. Turkeshi X. 2022. *Phys. Rev. B* 106:144313
71. Li Y, Chen X, Ludwig AWW, Fisher MPA. 2021. *Phys. Rev. B* 104(10):104305
72. Ippoliti M, Gullans MJ, Gopalakrishnan S, Huse DA, Khemani V. 2021. *Phys. Rev. X* 11:011030
73. Lavasani A, Alavirad Y, Barkeshli M. 2021. *Nat. Phys.* 17(3):342–47
74. Sang S, Hsieh TH. 2021. *Phys. Rev. Res.* 3(2):023200
75. Lavasani A, Alavirad Y, Barkeshli M. 2021. *Phys. Rev. Lett.* 127(23):235701
76. Lavasani A, Luo ZX, Vijay S. 2022. arXiv:2207.02877
77. Sriram A, Rakovszky T, Khemani V, Ippoliti M. 2022. arXiv:2207.07096
78. Vijay S. 2020. arXiv:2005.03052
79. Ippoliti M, Khemani V. 2021. *Phys. Rev. Lett.* 126(6):060501
80. Ippoliti M, Rakovszky T, Khemani V. 2022. *Phys. Rev. X* 12:011045
81. Lu TC, Grover T. 2021. *PRX Quantum* 2(4):040319
82. Alberton O, Buchhold M, Diehl S. 2021. *Phys. Rev. Lett.* 126(17):170602
83. Weinstein Z, Bao Y, Altman E. 2022. *Phys. Rev. Lett.* 129:080501
84. Buchhold M, Minoguchi Y, Altland A, Diehl S. 2021. *Phys. Rev. X* 11(4):041004

85. Jian SK, Liu C, Chen X, Swingle B, Zhang P. 2021. *Phys. Rev. Lett.* 127(14):140601
86. Lunt O, Pal A. 2020. *Phys. Rev. Res.* 2(4):043072
87. Lopez-Piqueres J, Ware B, Vasseur R. 2020. *Phys. Rev. B* 102(6):064202
88. Li Y, Vijay S, Fisher MPA. 2021. arXiv:2105.13352
89. Roy S, Chalker J, Gornyi I, Gefen Y. 2020. *Phys. Rev. Res.* 2(3):033347
90. McGinley M, Roy S, Parameswaran S. *Phys. Rev. Lett.* 129:090404
91. Turkeshi X, Dalmonte M, Fazio R, Schirò M. 2022. *Phys. Rev. B* 105(24):L241114
92. Sharma S, Turkeshi X, Fazio R, Dalmonte M. 2022. *SciPost Phys. Core* 5(2):023
93. Ochs W. 1975. *Rep. Math. Phys.* 8:109–20
94. Schuch N, Wolf MM, Verstraete F, Cirac JI. 2008. *Phys. Rev. Lett.* 100(3):030504
95. Weingarten D. 1978. *J. Math. Phys.* 19(5):999–1001
96. Collins B, Śniady P. 2006. *Commun. Math. Phys.* 264(3):773–95
97. Sekino Y, Susskind L. 2008. *J. High Energy Phys.* 2008(10):065
98. Lashkari N, Stanford D, Hastings M, Osborne T, Hayden P. 2013. *J. High Energy Phys.* 2013(4):22
99. Shenker SH, Stanford D. 2015. *J. High Energy Phys.* 2015(5):132
100. Khemani V, Vishwanath A, Huse DA. 2018. *Phys. Rev. X* 8(3):031057
101. Rakovszky T, Pollmann F, Von Keyserlingk C. 2018. *Phys. Rev. X* 8(3):031058
102. Chan A, De Luca A, Chalker J. 2018. *Phys. Rev. Lett.* 121(6):060601
103. Chan A, De Luca A, Chalker J. 2018. *Phys. Rev. X* 8(4):041019
104. Lazarides A, Das A, Moessner R. 2014. *Phys. Rev. E* 90:012110
105. D'Alessio L, Rigol M. 2014. *Phys. Rev. X* 4(4):041048
106. Ponte P, Chandran A, Papić Z, Abanin DA. 2015. *Ann. Phys.* 353:196–204
107. Plenio MB, Knight PL. 1998. *Rev. Mod. Phys.* 70:101–44
108. Gardiner C, Zoller P. 2004. *Quantum Noise: A Handbook of Markovian and Non-Markovian Quantum Stochastic Methods with Applications to Quantum Optics*. Berlin: Springer Sci. Bus. Media
109. Daley AJ. 2014. *Adv. Phys.* 63(2):77–149
110. Nagourney W, Sandberg J, Dehmelt H. 1986. *Phys. Rev. Lett.* 56(26):2797–99
111. Sauter T, Neuhauser W, Blatt R, Toschek PE. 1986. *Phys. Rev. Lett.* 57(14):1696–98
112. Bergquist JC, Hulet RG, Itano WM, Wineland DJ. 1986. *Phys. Rev. Lett.* 57(14):1699–702
113. Li J, Fan R, Wang H, Ye B, Zeng B, et al. 2017. *Phys. Rev. X* 7(3):031011
114. Yoshida B. 2021. arXiv:2109.08691
115. Fan R, Vijay S, Vishwanath A, You YZ. 2021. *Phys. Rev. B* 103(17):174309
116. Choi S, Bao Y, Qi XL, Altman E. 2020. *Phys. Rev. Lett.* 125(3):030505
117. Gullans MJ, Krastanov S, Huse DA, Jiang L, Flammia ST. 2021. *Phys. Rev. X* 11(3):031066
118. Oliveira R, Dahlsten OCO, Plenio MB. 2007. *Phys. Rev. Lett.* 98(13):130502
119. Znidaric M. 2008. *Phys. Rev. A* 78(3):032324
120. Hamma A, Santra S, Zanardi P. 2012. *Phys. Rev. Lett.* 109(4):040502
121. Zhou T, Nahum A. 2019. *Phys. Rev. B* 99(17):174205
122. Haake F. 1991. In *Quantum Coherence in Mesoscopic Systems*, ed. B Kramer, pp. 583–95. New York: Springer Sci. Bus. Media
123. Shannon CE. 1948. *Bell Syst. Tech. J.* 27(3):379–423
124. Sachdev S, Ye J. 1993. *Phys. Rev. Lett.* 70(21):3339–42
125. Kitaev A. 2014. Talk given at the *2015 Breakthrough Prize Fundamental Physics Symposium*, Stanford University, Palo Alto, CA, Nov. 10, 2014. **https://www.youtube.com/watch?v=OQ9qN8j7EZI**
126. Kos P, Ljubotina M, Prosen T. 2018. *Phys. Rev. X* 8(2):021062
127. Bertini B, Kos P, Prosen T. 2019. *Phys. Rev. Lett.* 123(21):210601
128. Brandao FG, Harrow AW, Horodecki M. 2016. *Commun. Math. Phys.* 346(2):397–434
129. Liu Y, Otten M, Bassirianjahromi R, Jiang L, Fefferman B. 2021. arXiv:2105.05232
130. Cross AW, Bishop LS, Sheldon S, Nation PD, Gambetta JM. 2019. *Phys. Rev. A* 100(3):032328
131. Bouland A, Fefferman B, Nirkhe C, Vazirani U. 2019. *Nat. Phys.* 15(2):159–63
132. Arute F, Arya K, Babbush R, Bacon D, Bardin JC, et al. 2019. *Nature* 574(7779):505–10
133. Aaronson S, Gunn S. 2019. arXiv:1910.12085

134. Kamenev A. 2011. *Field Theory of Non-Equilibrium Systems*. Cambridge, UK: Cambridge Univ. Press
135. Aleiner IL, Faoro L, Ioffe LB. 2016. *Ann. Phys.* 375:378–406
136. Dahlsten OCO, Oliveira R, Plenio MB. 2007. *J. Phys. A Math. Theor.* 40(28):8081–108
137. Harrow AW, Low RA. 2009. *Commun. Math. Phys.* 291:257–302
138. Zanardi P. 2014. *J. Math. Phys.* 55(8):082204
139. Hayden P, Nezami S, Qi XL, Thomas N, Walter M, Yang Z. 2016. *J. High Energy Phys.* 2016(11):9
140. Zhou T, Xu S, Chen X, Guo A, Swingle B. 2020. *Phys. Rev. Lett.* 124(18):180601
141. Vasseur R, Potter AC, You YZ, Ludwig AW. 2019. *Phys. Rev. B* 100(13):134203
142. Hunter-Jones N. 2019. arXiv:1905.12053
143. Liu H, Vardhan S. 2021. *PRX Quantum* 2:010344
144. Lieb EH, Robinson DW. 1972. In *Statistical Mechanics*. Springer, pp. 425–31.
145. Roberts DA, Stanford D, Susskind L. 2015. *J. High Energy Phys.* 2015(3):51
146. Roberts DA, Swingle B. 2016. *Phys. Rev. Lett.* 117:091602
147. Lubkin E. 1978. *J. Math. Phys.* 19(5):1028–31
148. Page DN. 1993. *Phys. Rev. Lett.* 71(23):3743
149. Nadal C, Majumdar SN, Vergassola M. 2011. *J. Stat. Phys.* 142(2):403–38
150. Mezei M. 2017. *J. High Energy Phys.* 2017(5):64
151. Jonay C, Huse DA, Nahum A. 2018. arXiv:1803.00089
152. Mezei M. 2018. *Phys. Rev. D* 98(10):106025
153. Mezei M, Virrueta J. 2020. *J. High Energy Phys.* 2020(2):13
154. Nahum A, Ruhman J, Huse DA. 2018. *Phys. Rev. B* 98(3):035118
155. Rakovszky T, von Keyserlingk C, Pollmann F. 2019. *Phys. Rev. B* 100(12):125139
156. Gong Z, Nahum A, Piroli L. 2022. *Phys. Rev. Lett.* 128(8):080602
157. Swingle B. 2012. *Phys. Rev. D* 86(6):065007
158. Chamon C, Mucciolo ER. 2012. *Phys. Rev. Lett.* 109(3):030503
159. Perez-Garcia D, Verstraete F, Wolf M, Cirac J. 2007. *Quantum Inf. Comput.* 7(5–6):401–30
160. Verstraete F, Murg V, Cirac JI. 2008. *Adv. Phys.* 57(2):143–224
161. Casini H, Liu H, Mezei M. 2016. *J. High Energy Phys.* 2016(7):77
162. Huse DA, Henley CL, Fisher DS. 1985. *Phys. Rev. Lett.* 55(26):2924
163. Kardar M, Parisi G, Zhang YC. 1986. *Phys. Rev. Lett.* 56(9):889–92
164. Halpin-Healy T, Takeuchi KA. 2015. *J. Stat. Phys.* 160(4):794–814
165. Corwin I. 2012. *Random Matrices: Theory Appl.* 1(01):1130001
166. Kriecherbauer T, Krug J. 2010. *J. Phys.: Math. Theor.* 43(40):403001
167. Harrow AW. 2013. arXiv:1308.6595
168. Bertini B, Kos P, Prosen T. 2019. *Phys. Rev. X* 9(2):021033
169. Bao Y, Choi S, Altman E. 2021. *Ann. Phys.* 435:168618
170. Rakovszky T, Pollmann F, Von Keyserlingk C. 2019. *Phys. Rev. Lett.* 122(25):250602
171. Huang Y. *IOP SciNotes* 1(3):035205
172. Zhou T, Ludwig AW. 2020. *Phys. Rev. Res.* 2(3):033020
173. Feldmeier J, Sala P, De Tomasi G, Pollmann F, Knap M. 2020. *Phys. Rev. Lett.* 125(24):245303
174. Gromov A, Lucas A, Nandkishore RM. 2020. *Phys. Rev. Res.* 2(3):033124
175. Ryu S, Takayanagi T. 2006. *Phys. Rev. Lett.* 96(18):181602
176. Shenker SH, Stanford D. 2014. *J. High Energy Phys.* 2014(3):67
177. Shenker SH, Stanford D. 2014. *J. High Energy Phys.* 2014(12):46
178. Maldacena J, Shenker SH, Stanford D. 2016. *J. High Energy Phys.* 2016(8):106
179. Stanford D. 2016. *J. High Energy Phys.* 2016(10):9
180. Gu Y, Qi XL, Stanford D. 2017. *J. High Energy Phys.* 2017(5):125
181. Roberts DA, Swingle B. 2016. *Phys. Rev. Lett.* 117(9):091602
182. Swingle B, Chowdhury D. 2017. *Phys. Rev. B* 95(6):060201
183. Huang Y, Zhang YL, Chen X. 2017. *Ann. Phys.* 529(7):1600318
184. Chen X, Zhou T, Huse DA, Fradkin E. 2017. *Ann. Phys.* 529(7):1600332
185. Chen Y. 2016. arXiv:1608.02765

186. He RQ, Lu ZY. 2017. *Phys. Rev. B* 95(5):054201
187. Fan R, Zhang P, Shen H, Zhai H. 2017. *Sci. Bull.* 62(10):707–11
188. Dóra B, Moessner R. 2017. *Phys. Rev. Lett.* 119(2):026802
189. Fortes EM, García-Mata I, Jalabert RA, Wisniacki DA. 2019. *Phys. Rev. E* 100(4):042201
190. McGinley M, Nunnenkamp A, Knolle J. 2019. *Phys. Rev. Lett.* 122(2):020603
191. Yan H, Wang JZ, Wang WG. 2019. *Commun. Theor. Phys.* 71(11):1359
192. Zhu G, Hafezi M, Grover T. 2016. *Phys. Rev. A* 94(6):062329
193. Swingle B, Bentsen G, Schleier-Smith M, Hayden P. 2016. *Phys. Rev. A* 94(4):040302
194. Yao NY, Grusdt F, Swingle B, Lukin MD, Stamper-Kurn DM, et al. 2016. arXiv:1607.01801
195. Gärttner M, Bohnet JG, Safavi-Naini A, Wall ML, Bollinger JJ, Rey AM. 2017. *Nat. Phys.* 13(8):781–86
196. Nahum A, Roy S, Vijay S, Zhou T. 2022. arXiv:2205.11544
197. Kos P, Bertini B, Prosen T. 2021. *Phys. Rev. X* 11:011022
198. von Keyserlingk C, Pollmann F, Rakovszky T. 2022. *Phys. Rev. B* 105:245101
199. Rakovszky T, von Keyserlingk C, Pollmann F. 2022. *Phys. Rev. B* 105(7):075131
200. Iaconis J, Vijay S, Nandkishore R. 2019. *Phys. Rev. B* 100(21):214301
201. Pai S, Pretko M, Nandkishore RM. 2019. *Phys. Rev. X* 9(2):021003
202. Pai S, Pretko M, Nandkishore RM. 2019. *Phys. Rev. X* 9(4):049901
203. Khemani V, Hermele M, Nandkishore R. 2020. *Phys. Rev. B* 101(17):174204
204. Sala P, Rakovszky T, Verresen R, Knap M, Pollmann F. 2020. *Phys. Rev. X* 10:011047
205. Feldmeier J, Knap M. 2021. *Phys. Rev. Lett.* 127(23):235301
206. Feldmeier J, Witczak-Krempa W, Knap M. 2022. *Phys. Rev. B* 106:094303
207. Lerose A, Sonner M, Abanin DA. 2021. *Phys. Rev. X* 11(2):021040
208. Chandran A, Laumann C. 2015. *Phys. Rev. B* 92(2):024301
209. Lazarides A, Das A, Moessner R. 2015. *Phys. Rev. Lett.* 115:030402
210. Ponte P, Papić Z, Huveneers F, Abanin DA. 2015. *Phys. Rev. Lett.* 114(14):140401
211. Garratt S, Chalker J. 2021. *Phys. Rev. Lett.* 127(2):026802
212. Farshi T, Toniolo D, González-Guillén CE, Alhambra ÁM, Masanes L. 2022. *J. Math. Phys.* 63(3):032201
213. Khemani V, Lazarides A, Moessner R, Sondhi SL. 2016. *Phys. Rev. Lett.* 116(25):250401
214. Else DV, Bauer B, Nayak C. 2016. *Phys. Rev. Lett.* 117(9):090402
215. Nathan F, Abanin D, Berg E, Lindner NH, Rudner MS. 2019. *Phys. Rev. B* 99(19):195133
216. Titum P, Berg E, Rudner MS, Refael G, Lindner NH. 2016. *Phys. Rev. X* 6(2):021013
217. Harper F, Roy R, Rudner MS, Sondhi S. 2020. *Annu. Rev. Condens. Matter Phys.* 11:345–68
218. Bohigas O, Giannoni MJ, Schmit C. 1984. *Phys. Rev. Lett.* 52:1
219. Bertini B, Kos P, Prosen T. 2018. *Phys. Rev. Lett.* 121(26):264101
220. Bertini B, Kos P, Prosen T. 2021. *Commun. Math. Phys.* 387:597–620
221. Flack A, Bertini B, Prosen T. 2020. *Phys. Rev. Res.* 2(4):043403
222. Mehta ML. 2004. *Random Matrices*, Vol. 142, *Pure and Applied Matematics*. Amsterdam: Elsevier. 3rd ed.
223. Cotler J, Hunter-Jones N, Liu J, Yoshida B. 2017. *J. High Energy Phys.* 2017(11):48
224. Liu M, Liu J, Alexeev Y, Jiang L. 2022. arXiv:2205.09900
225. Prange R. 1997. *Phys. Rev. Lett.* 78(12):2280
226. Garratt S, Chalker J. 2021. *Phys. Rev. X* 11(2):021051
227. Chan A, Shivam S, Huse DA, De Luca A. 2021. arXiv:2109.04475
228. Gopalakrishnan S, Lamacraft A. 2019. *Phys. Rev. B* 100(6):064309
229. Reid I, Bertini B. 2021. *Phys. Rev. B* 104:014301
230. Bertini B, Kos P, Prosen T. 2020. *SciPost Phys.* 8(4):067
231. Piroli L, Bertini B, Cirac JI, Prosen T. 2020. *Phys. Rev. B* 101(9):094304
232. Zhou T, Harrow AW. 2022. *Phys. Rev. B* 106:L201104
233. Ho WW, Choi S. 2022. *Phys. Rev. Lett.* 128(6):060601
234. Fritzsch F, Prosen T. 2021. *Phys. Rev. E* 103(6):062133
235. Claeys PW, Lamacraft A. 2021. *Phys. Rev. Lett.* 126(10):100603
236. Jonay C, Khemani V, Ippoliti M. 2021. *Phys. Rev. Res.* 3(4):043046
237. Harris RJ, McMahon NA, Brennen GK, Stace TM. 2018. *Phys. Rev. A* 98(5):052301

238. Berger J, Osborne TJ. 2018. arXiv:1804.03199
239. Doroudiani M, Karimipour V. 2020. *Phys. Rev. A* 102:012427
240. Borsi M, Pozsgay B. 2022. *Phys. Rev. B* 106:014302
241. Banuls MC, Hastings MB, Verstraete F, Cirac JI. 2009. *Phys. Rev. Lett.* 102(24):240603
242. Akila M, Waltner D, Gutkin B, Guhr T. 2016. *J. Phys. A Math. Theor.* 49(37):375101
243. Piroli L, Pozsgay B, Vernier E. 2017. *Nuclear Phys. B* 925:362–402
244. Gottesman D. 1996. *Phys. Rev. A* 54(3):1862–68
245. Aaronson S, Gottesman D. 2004. *Phys. Rev. A* 70(5):052328
246. Webb Z. 2016. *Quantum Inf. Comput.* 16(15–16):1379–400
247. Zhu H. 2017. *Phys. Rev. A* 96(6):062336
248. Zhou T, Chen X. 2019. *Phys. Rev. E* 99(5):052212
249. Xu S, Swingle B. 2019. *Phys. Rev. X* 9(3):031048
250. Rowlands DA, Lamacraft A. 2018. *Phys. Rev. B* 98(19):195125
251. Bauer M, Bernard D, Jin T. 2019. *SciPost Phys.* 6(4):045
252. Bernard D, Jin T. 2019. *Phys. Rev. Lett.* 123(8):080601
253. Bernard D, Piroli L. 2021. *Phys. Rev. E* 104:014146
254. Iaconis J, Vijay S, Nandkishore R. 2019. *Phys. Rev. B* 100(21):214301
255. Iaconis J, Lucas A, Nandkishore R. 2021. *Phys. Rev. E* 103(2):022142
256. Richter J, Pal A. 2022. *Phys. Rev. Res.* 4:L012003
257. Singh H, Ware BA, Vasseur R, Friedman AJ. 2021. *Phys. Rev. Lett.* 127(23):230602
258. Iaconis J, Lucas A, Chen X. 2020. *Phys. Rev. B* 102(22):224311
259. Gopalakrishnan S. 2018. *Phys. Rev. B* 98(6):060302(R)
260. Klobas K, Bertini B, Piroli L. 2021. *Phys. Rev. Lett.* 126(16):160602
261. Klobas K, Bertini B. 2021. *SciPost Phys.* 11(6):106
262. Lopez-Piqueres J, Gopalakrishnan S, Vasseur R. 2022. *J. Phys. A Math. Theor.* 55:234005
263. Kuniba A, Misguich G, Pasquier V. 2020. *J. Phys. A Math. Theor.* 53(40):404001
264. Iadecola T, Vijay S. 2020. *Phys. Rev. B* 102(18):180302
265. Rozon PG, Gullans MJ, Agarwal K. 2021. arXiv:2112.12153
266. Gopalakrishnan S, Zakirov B. 2018. *Quantum Sci. Technol.* 3(4):044004
267. Gopalakrishnan S, Huse DA, Khemani V, Vasseur R. 2018. *Phys. Rev. B* 98(22):220303
268. Alba V, Dubail J, Medenjak M. 2019. *Phys. Rev. Lett.* 122(25):250603
269. Aharonov D. 2000. *Phys. Rev. A* 62(6):062311
270. Sierant P, Turkeshi X. 2022. *Phys. Rev. Lett.* 128(13):130605
271. Bonnes L, Läuchli AM. 2014. arXiv:1411.4831
272. Garrahan JP, Lesanovsky I. 2010. *Phys. Rev. Lett.* 104(16):160601
273. Cardy J. 1996. *Scaling and Renormalization in Statistical Physics*. Vol. 5, *Cambridge Lect. Notes Phys.* Cambridge, UK: Cambridge Univ. Press
274. Amit DJ. 1976. *J. Phys. A Math. Gen.* 9(9):1441
275. Shepherd D, Bremner MJ. 2009. *Proc. R. Soc. A Math. Phys. Eng. Sci.* 465(2105):1413–39
276. Bremner MJ, Jozsa R, Shepherd DJ. 2011. *Proc. R. Soc. A Math. Phys. Eng. Sci.* 467(2126):459–72
277. Bollobás B. 1998. In *Modern Graph Theory*, ed. S Axler, FW Gehring, KA Ribet, pp. 215–52. New York: Springer Sci. Bus. Media
278. Li Y, Fisher MPA. 2021. arXiv:2108.04274
279. Huse DA, Nandkishore R, Oganesyan V, Pal A, Sondhi SL. 2013. *Phys. Rev. B* 88:014206
280. Pekker D, Refael G, Altman E, Demler E, Oganesyan V. 2014. *Phys. Rev. X* 4:011052
281. Agrawal U, Zabalo A, Chen K, Wilson JH, Potter AC, et al. 2022. *Phys. Rev. X* 12:041002
282. Barratt F, Agrawal U, Gopalakrishnan S, Huse DA, Vasseur R, Potter AC. 2022. *Phys. Rev. Lett.* 129:120604
283. Kitaev AY. 2003. *Ann. Phys.* 303:2–30
284. Kitaev A, Preskill J. 2006. *Phys. Rev. Lett.* 96(11):110404
285. Levin M, Wen XG. 2006. *Phys. Rev. Lett.* 96(11):110405
286. Jian CM, Bauer B, Keselman A, Ludwig AWW. 2022. *Phys. Rev. B* 106:134206

287. Fidkowski L, Haah J, Hastings MB. 2021. *Quantum* 5:382
288. Turkeshi X, Piroli L, Schirò M. 2022. *Phys. Rev. B* 106:024304
289. Neill C, Roushan P, Kechedzhi K, Boixo S, Isakov SV, et al. 2018. *Science* 360(6385):195–99
290. Aaronson S, Chen L. 2017. In *Proceedings of the 32nd Computational Complexity Conference, Riga, Latvia, July 6–9*, Art. No. 22. **https://dl.acm.org/doi/10.5555/3135595.3135617**
291. Boixo S, Isakov SV, Smelyanskiy VN, Babbush R, Ding N, et al. 2018. *Nat. Phys.* 14(6):595–600
292. Ippoliti M, Kechedzhi K, Moessner R, Sondhi S, Khemani V. 2021. *PRX Quantum* 2(3):030346
293. Islam R, Ma R, Preiss PM, Tai ME, Lukin A, et al. 2015. *Nature* 528(7580):77–83
294. Kaufman AM, Tai ME, Lukin A, Rispoli M, Schittko R, et al. 2016. *Science* 353(6301):794–800
295. Daley A, Pichler H, Schachenmayer J, Zoller P. 2012. *Phys. Rev. Lett.* 109(2):020505
296. Alves CM, Jaksch D. 2004. *Phys. Rev. Lett.* 93(11):110501
297. Smith J, Lee A, Richerme P, Neyenhuis B, Hess PW, et al. 2016. *Nat. Phys.* 12(10):907–11
298. Choi J-Y, Hild S, Zeiher J, Schauß P, Rubio-Abadal A, et al. 2016. *Science* 352(6293):1547–52
299. Lukin A, Rispoli M, Schittko R, Tai ME, Kaufman AM, et al. 2019. *Science* 364(6437):256–60
300. Bernien H, Schwartz S, Keesling A, Levine H, Omran A, et al. 2017. *Nature* 551(7682):579–84
301. Kinoshita T, Wenger T, Weiss DS. 2006. *Nature* 440(7086):900–3
302. Tang Y, Kao W, Li KY, Seo S, Mallayya K, et al. 2018. *Phys. Rev. X* 8(2):021030
303. Mi X, Roushan P, Quintana C, Mandrà S, Marshall J, et al. 2021. *Science* 374(6574):1479–83
304. Satzinger KJ, Liu YJ, Smith A, Knapp C, Newman M, et al. 2021. *Science* 374(6572):1237–41
305. Mi X, Ippoliti M, Quintana C, Greene A, Chen Z, et al. 2021. *Nature* 601(7894):531–36
306. Noel C, Niroula P, Zhu D, Risinger A, Egan L, et al. 2022. *Nat. Phys.* 18:760–64
307. Koh JM, Sun SN, Motta M, Minnich AJ. 2022. arXiv:2203.04338
308. Noh K, Jiang L, Fefferman B. 2020. *Quantum* 4:318
309. Li Z, Sang S, Hsieh TH. 2022. arXiv:2203.16555
310. Hastings MB, Haah J. 2021. *Quantum* 5:564
311. Aasen D, Wang Z, Hastings MB. 2022. *Phys. Rev. B* 106:085122